BATTERY MODULE THERMAL MANAGEMENT SYSTEM DESIGN

TESTING AND THERMAL MANAGEMENT SYSTEM DESIGN OF AN ULTRA-FAST CHARGING BATTERY MODULE FOR ELECTRIC VEHICLES

BY

ZIYU ZHAO, B.A.Sc

A THESIS

SUBMITTED TO THE DEPARTMENT OF MECHANICAL ENGINEERING

AND THE SCHOOL OF GRADUATE STUDIES

OF MCMASTER UNIVERSITY

IN PARTIAL FULFILMENT OF THE REQUIREMENTS

FOR THE DEGREE OF

Master of Applied Science

Master of Applied Science (2021) McMaster University

(mechanical engineering) Hamilton, Ontario, Canada

TITLE:	Testing and Thermal Management System Design of an Ultra-Fast Charging Battery Module for Electric Vehicles
AUTHOR:	Ziyu Zhao B.A.Sc. (Mechanical Engineering Automotive Option) McMaster University, Hamilton, Canada
SUPERVISOR:	Dr. Ali Emadi
NUMBER OF PAGES:	xix, 115

Lay Abstract

With a demanding market of electric vehicles, battery technologies have grown rapidly in recent years. Among all the battery research topics, the development of ultra-fast charging, that can fully charge the battery pack within 15 minutes, is the most promising direction to address the range anxiety and improve the social acceptance of electric vehicles. Nevertheless, the application of ultra-fast charging has many challenges. In particular, an efficient thermal management system is significant to guarantee the safety and prolong the service life of the battery pack. This thesis contributes to study the fundamentals of the battery field, and design liquid cooling systems to observe the thermal behavior of a battery prototype module under fast charging and general use. FEA thermal modeling of the battery module is developed to provide a guide for further test validation.

Abstract

Traditional vehicles with internal combustion engines have resulted in severe environmental pollution, which motivates the development of electric vehicles and hybrid electric vehicles. Due to the low energy density and long refueling time of the battery pack, it is still hard for electric vehicles and hybrid electric vehicles to be widely accepted by consumers. As the batteries with a better ultra-fast charging capability are massively produced, the range anxiety issue is somewhat alleviated.

During a charging with a large current magnitude, the battery generally has a great amount of heat generation and evident temperature rise. Therefore, a thermal management system is necessary to effectively dissipate the battery loss and minimize the degradation mechanisms caused by extreme temperature. The motivation of this thesis is to study the discipline of the battery thermal management system as an application for electric vehicles. The design methodologies are presented in both experiment tests and numerical simulation.

For the comparative study between active liquid cooling methods for a lithium-ion battery module using experimental techniques, two battery modules with three Kokam Nickel Manganese Cobalt battery cells connected in parallel are developed. One has liquid coolant flowing along the edge of the model, and another with liquid coolant flowing between the cells. Several characterization tests, including thermal

resistance tests, fast charging tests up to 5C, and drive cycle tests are designed and performed on the battery module. The inter-cell cooling module has a lower peak temperature rise and faster thermal response compared to the edge cooling module, i.e., 4.1°C peak temperature rise under 5C charging for the inter-cell cooling method and 14.2°C for the edge cooling method.

The thermal models built in ANSYS represent the numerical simulation of the inter-cell cooling module as a comparison with the experiment. A cell loss model is developed to calculate the battery heat generation rate under ultra-fast charging tests and a road trip test, which are further adopted as the inputs to the thermal models. The simulation of the 5C ultra-fast charging test gives the peak temperature rise just 0.47°C lower than the experimental measurement, it indicates that the FEA thermal models can provide an accurate temperature prediction of the battery module.

To my family, home is where you are.

To my friends, the creed I grow with.

Acknowledgements

The pandemic COVID-19 has been prevailing for more than a year, and hardly can we see its tail. It is difficult to conduct the work for this thesis during this tough period. Nonetheless, with the assistant of my family, friends, colleagues, and mentors, finally I am able to accomplish this research work in time. I would like to express my paramount appreciation to all the people that helped me with the thesis.

First of all, thank you to my supervisor, Dr. Ali Emadi. It is one of the greatest milestones in my life that I was admitted as a Mechanical Engineering master student by McMaster University and became a part of the team at McMaster Automotive Resource Centre. You brought my journey here so that I could meet these prominent figures and learned impressive lessons.

Thank you to Dr. Phillip J. Kollmeyer, you are a knowledgeable and patient person. I am so grateful that you always spare time to answer my questions. Thank you for providing me with many ideas and aids that encourage my thesis and research. Also, thank you to Dr. Saeid Habibi and Cam Fisher, you offered me the test facilities and experimental supports in Mechatronics and Hybrid Technology battery laboratory.

Special thanks to Jeremy M. Lempert and Melissa He, I started the research of battery thermal management system on the basis of your previous contributions.

Jeremy had great work building the cell loss model and FEA thermal models for the edge cooling battery module, which are referred in this thesis. The edge cooling battery module with the cell selection was designed and fabricated by Melissa.

Many thanks to my colleagues in the battery energy management system team under the joint Stellantis-McMaster Car of the Future Project, I learned lots of battery knowledge and professional skills from you. Also thank you to all the classmates and friends I met at McMaster University, the time would be much less interesting without you.

Lastly and deep inside, I would like to thank my family, my kindest mother and strictest father. If it were not for your love and dedication, I would not be here exploring the magnificent world.

Contents

List of Figures

List of Tables

Abbreviations

AC	Alternating Current
BMS	Battery Management System
CAD	Computer-Aided Design
CAE	Computer-Aided Engineering
CAN	Controller Area Network
CCS	Combined Charging System
CFD	Computational Fluid Dynamics
CHAdeMO	CHArge de MOve
CID	Charge Interrupt Device
DC	Direct Current
DOD	Depth of Discharge
ECM	Equivalent Circuit Model
EV	Electric Vehicle

FEA	Finite Element Analysis
HEV	Hybrid Electric Vehicle
HPPC	Hybrid Pulse Power Characterization
ICE	Internal Combustion Engine
LCO	Lithium Cobalt Oxide
LFP	Lithium Iron Phosphate
Li-ion	Lithium-Ion
LIN	Local Interconnect Network
LMO	Lithium Manganese Oxide
NCA	Nickel Cobalt Aluminum
NiCd	Nickel-Cadmium
NiMH	Nickel-Metal Hydride
NMC	Nickel Manganese Cobalt
OCV	Open-Circuit Voltage
PCM	Phase Change Materials
PTC	Positive Thermal Coefficient
SAE	Society of Automotive Engineers
SEI	Solid Electrolyte Interface

SMBus	System Management Bus
SOC	State of Charge
SOH	State of Health
TMS	Thermal Management System

Statement of Authorship

I hereby declare that I am the sole author of this master thesis. The materials contained in Chapter 4 is adapted from the ITEC 2021 conference paper as following:

Z. Zhao, P. J. Kollmeyer, J. M. Lempert and A. Emadi, "Experimental Comparison of Two Liquid Cooling Methods for Ultrafast Charging Lithium-Ion Battery Modules," 2021 IEEE Transportation Electrification Conference & Expo (ITEC), 2021, pp. 46-51, doi: 10.1109/ITEC51675.2021.9490034.

The major contributions to the paper are the work performed by the first author, Ziyu Zhao. The first author was responsible for the literature review, design and performance of the experiment, discussion and conclusion, primary manuscript. Dr. Phillip J. Kollmeyer provided the experimental apparatus, technical support and suggestions, revisions. Jeremy M. Lempert and Melissa He offered the design and fabrication of the edge cooling battery module. Dr. Ali Emadi and industrial partner Stellantis N.V. contributed to the funding and proofreading of the paper.

Chapter 5 cited some work from my colleague, Jeremy M. Lempert, and his published journal paper. The entropic heating coefficient map was generated by his elaborated experiment, this thesis work utilizes his map with updated characterization data of the battery module for the cell loss calculation.

Chapter 1

Introduction

1.1 Background and Motivation

An elaborate transportation network has brought incredible mobility convenience to human being and good, whereas the transportation system takes the largest part of the total energy consumption. Among all the transportation means including road, railway, ships, and aviation, road transportation especially automobiles holds most of the energy spent (Singh *et al.*, 2019). Considering that vehicles with an internal combustion engine (ICE) are still the mainstream in the automobile industry, the resultant emission pollution of greenhouse gases, NO_2, NO, CO, etc. have caused increasing environmental degradation and harm to human health (Thomas, 2009).

With the increasing awareness of environmental issues, the advantages of hybrid electric vehicles (HEVs) and electric vehicles (EVs) have drawn unprecedented public attention. The automotive industry is undergoing a revolution from traditional vehicles with ICEs to sustainable vehicles with new energy storage systems. For EVs and HEVs, lithium-ion (Li-ion) chemistry batteries are considered the most viable energy

storage device for these electrified powertrains (Spotnitz, 2005). Battery technology plays a key role in developing clean, fuel-efficient HEVs and EVs (Chalk and Miller, 2006), with high specific energy and power density batteries enabling the development of longer range and faster charging vehicles.

However, EVs and HEVs are still confronted with many challenges that prevent them from a wide social acceptance. A vehicle with the battery as a power source generally has a high capital cost, although the running cost is low (Andwari *et al.*, 2017). More importantly, range anxiety is an indelible barrier: an EV usually has a lower cruise range than a conventional vehicle, and charging the battery takes quite a while. Consequently, the customers have the fear of pulling over during their trips. Besides, an insufficient charging infrastructure aggravates this problem (Andwari *et al.*, 2017; Kumar and Revankar, 2017).

Many researchers and battery suppliers endeavor to develop battery technology with a higher energy and power density, longer cycle life (Lu *et al.*, 2013). One important character of the battery that can address the range anxiety is ultra-fast charging. The Society of Automotive Engineers in the US defined standard J1772 with direct current charging as 200-450V and up to 80A and 200A for levels 1 and 2, respectively, which can provide a maximum power of around 50kW to extend the EVs by 60-80 miles of driving range by charging for 20 minutes (Doll, 2021; Liu *et al.*, 2019). The Tesla Supercharger has 480V DC offering a charging rate of 120kW so that Tesla vehicles can be refueled for 200 miles driving range in less than 30 minutes. The US Advanced Battery Consortium sets up the goal for charging the low-cost/fast-charge EV batteries to 80% of the pack capacity within 15 minutes in 2023 (Liu *et al.*, 2019).

The automotive industry has been putting the priority of work into the development of EVs and HEVs, as the core technology of the electrified powertrain, battery applications have been making burgeoning progress. For the demanding applications to EVs and HEVs, the batteries are vulnerable to many physical effects like pressure, vibration, and temperature (Wu *et al.*, 2019). Although pressure and vibration issues can be handled by the well-designed housing of vehicle chassis, the temperature control requires a critical system design considering both housing configuration and parasitic power consumption. In fact, the temperature is the key factor that affects battery performance.

In general, a low temperature will increase the charge transfer resistance of the graphite and cathode so that the charging of a battery at a low State of Charge (SOC) becomes difficult, hence the power and energy of batteries are depressed at low temperature (Zhang *et al.*, 2003). In addition to an elevated temperature, the battery ohmic impedance increases rapidly by the ununiform solid electrolyte interface (SEI) and the electrolyte decomposition, thus resulting in a significant capacity fading (Shim *et al.*, 2002). Moreover, for a battery pack application, the maldistribution of the temperature across the batteries will result in asynchronous electrochemical reactions, which further causes cell unbalancing (Wu *et al.*, 2019).

Under ultra-fast charging, a battery has a large current and polarization reactions, a high rate of heat generation is usually observed. Therefore, an effective thermal management system (TMS) needs to be designed and developed to control the battery temperature within the desired range. The purpose of this thesis is to study the thermal behavior of a battery module with ultra-fast charging capabilities. Subsequently, a liquid cooling system both in the experiment and numerical simulation is

designed to validate practical applications of daily driving and ultra-fast charging.

1.2 Contributions

The significance of this thesis is to present experimental and modeling methodologies for a battery module. The thermal management module is designed to investigate the battery temperature behavior under high C rate charging and emulation of drive cycles.

This work begins with the concept from relevant literature review regarding degradation mechanisms of ultra-fast charging, and the research of battery TMS. Then three commercial pouch cells connected in parallel are characterized and used for cooling modules design. Two liquid cooling modules are designed with different heat flow configurations, their cooling performance are compared in the experiments under a series of ultra-fast charging tests and road trip test. Furthermore, a heat generation model is applied to simulate the cell loss as the input to the thermal modeling. The thermal model of one liquid cooling module is built, the experimental tests are replicated on the thermal model to compare the thermal modeling accuracy.

The innovative contributions of this thesis include developing, testing, and comparing two liquid cooling battery modules since there is not much experimental discussion and investigation of the battery applications on EVs. In addition, the corresponding FEA thermal models can give an accurate temperature estimation of the battery module, thus they are beneficial to serve as guidance for further experimental validation.

1.3 Thesis Outline

This thesis consists of three main objectives: fundamental and literature review of EV batteries, experimental development, and validation of two liquid cooling battery modules, thermal modeling and comparison of the inter-cell cooling battery module. The outline of the content is composed as the following:

The present chapter as Chapter 1 defines the background of the battery applications on EVs and HEVs, which leads to the motivation of this thesis to study battery TMS. The main contributions and outline of the thesis are presented at the end of the chapter.

Chapter 2 discusses the battery fundamentals, definitions, and management system. This chapter states the basic knowledge in the field of battery and lays the foundation for the following battery research.

Chapter 3 conducts the literature review of battery ultra-fast charging state of art, fast charging infrastructure, and three main degradation mechanisms are introduced. Then battery TMS state of art is presented by summarizing involved research work and providing relevant industrial examples.

In Chapter 4, the details of developing two liquid cooling battery modules and experimental apparatus are shown. The description of electrical and thermal characterization tests is presented. By carrying out these tests on the edge cooling module and the inter-cell cooling module, the cooling performances of the two modules are compared and discussed.

Chapter 5 is the development of the thermal modeling of the inter-cell cooling battery module. Initially, the theoretical basis of heat generation and battery loss model is given by considering both reversible and irreversible loss. With all the

measured data and cited entropic heating coefficient map, the losses of ultra-fast charging and road trip tests are calculated. Secondly, the CFD-based steady state model and thermal-only transient state model are established in ANSYS, a mesh sensitivity study is performed on the thermal models to check the meshing quality.

The thermal models of the inter-cell cooling module are validated in Chapter 6 by replicating the tests from the experiment. Afterward, the simulation results are benchmarked against the experimental measurements to assess the thermal modeling accuracy.

Eventually, conclusions are drawn in Chapter 7. The thesis work is summarized by compiling the findings and results of each chapter. Moreover, the recommendation and future work as the extension of this thesis are pointed out.

Chapter 2

Battery Fundamentals, Definitions, and Management System

2.1 Battery Fundamentals

2.1.1 Battery Operation

A Battery is an electrochemical device that can achieve the energy conversion between chemical energy and electrical energy. A battery is composed of three elements: a cathode, an anode, and electrolyte as the catalyst (Battery University, 2018a). The energy conversion occurs when the oxidation-reduction reaction between the two electrodes takes place and an electromotive force is produced. When a battery is being charged, the positive ions are generated at the cathode and electrolyte interface, which results in a driving force of the electrons towards the cathode. As the electrons move to the cathode, a voltage potential exists between the cathode and the anode. When the battery is discharging, the voltage potential leads the current to flow from the

cathode through the external loads and go back to the anode; when charging, the current flows in the opposite direction. A typical schematic of the battery discharge and charge is shown in Figure 2.1.

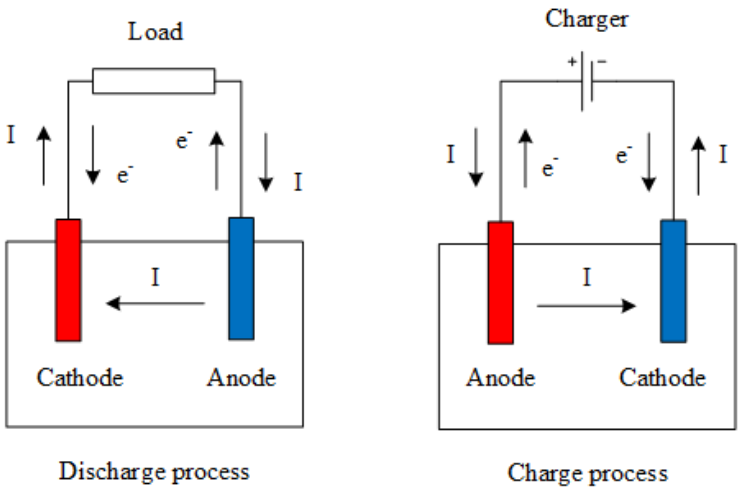

Figure 2.1: Battery electrochemical operation (BioLogic, 2021)

2.1.2 Battery Construction

Anode and Cathode

The anode is of a battery the electrode that releases electrons and the oxidation reaction occurs during discharge; the cathode is the other electrode that absorbs the electrons and the reduction reaction occurs. The conventional current is a result of the electron flow, and it has the opposite direction of the electron movements. Therefore, the anode is the electrode that the conventional current enters the polarized battery, the cathode is the electrode that the conventional current leaves the battery. Different from the convention that the anode is the terminal that current flows in to, as the battery is an energy storage system and provides electric power, the anode of a

battery is always negative, while the cathode is always positive. Generally, the anode of a battery is made of graphitic carbon, and the cathode is made of metal oxide. The material of the cathode determines the battery chemistry, e.g., lithium cobalt oxide (LCO) battery, lithium manganese oxide (LMO) battery, lithium nickel cobalt aluminum oxide (NCA) battery, lithium iron phosphate (LFP) battery, lithium nickel manganese cobalt oxide (NMC) battery.

Electrolyte and Separator

The electrolyte is an activator of the ion flow to support the electrochemical reaction. When the electrolyte is dissolved in a polar solvent, they are separated into cations and anions, an electrically conducting solution is produced. If an electric potential is applied to the solution, the cations are drawn to the electrode that has abundant electrons. A wet-cell battery contains a liquid electrolyte such as sulfuric acid, the liquid electrolyte can move freely between the electrodes. In a dry-cell battery, the electrolyte is added to the separator in a moistened form, the separator as an insulating divider separates the two electrodes physically by allowing free positive ion flow but preventing electron flow.

2.1.3 Battery Classification by Function

When the function of a battery is concerned, the electrochemical battery has three main categories as primary battery, secondary battery, and reserve battery (Washington Edu, 2021).

Primary Battery

A primary battery cannot be recharged and should be disposable after a single discharge. Inside the primary battery, an irreversible chemical reaction is produced

within the electrodes to generate electricity. The electrolyte of most primary batteries is absorbent material or has a separator, therefore, they are mainly termed as dry cells. Any attempt to recharge a primary cell will result in the leaking of hazardous liquid or material.

Secondary Battery

A secondary battery is commonly referred to as the one that can be electrically recharged after discharge and is able to return to its pre-discharge status. It involves a reversible chemical reaction of charging that is opposite to discharging within the battery. The secondary battery has two main intended applications. The first one is to be used as an energy storage device to deliver power. In most cases, it is connected to the primary power source to be charged, and it is used or discharged on demand. Application examples include emergency lamp, aircraft system, and some propulsion system for load leveling. The other type functions as the primary battery, but it can be recharged for another usage. This type includes examples of portable consumer electronics and EV power sources.

Reserve Battery

Different from the primary and secondary battery, a reserve battery has the key component such as the electrolyte isolated from the remaining components in the battery, and it is activated prior to usage. This type of battery is widely used in thermal batteries, where the electrolyte is not activated until the temperature reaches its melting point, then the electrolyte transforms from the solid state into the liquid state to allow for ionic conduction. Reserve battery is commonly used in the situation where the self-discharge phenomenon needs to be significantly minimized. There are four main activation methods for the reserve battery: water activation, electrolyte

activation, gas activation, and heat activation. Reserve battery is mostly used in timing, temperature, and pressure sensitive military detonation system and life vest applications.

2.1.4 Battery Classification by Chemistry

Depending on the composition material of a battery, most secondary batteries are lead-, nickel- and lithium-based. In electrified vehicles, there are three main types of batteries applied: Lead-Acid, Nickel-Metal Hydride (NiMH), and Li-ion.

Lead-Acid Battery

In 1859, the lead-acid battery was invented by the French physician Gaston Planté, it was the earliest commercial use of a rechargeable battery. With mature technology, lead-acid battery is highly reliable and delivers bulk power as cheaply as other battery chemistries cannot compete, it has a relatively large power to weight ratio thus can supply high surge currents. However, the lead acid battery is heavy and not suitable for deep cycling. A lead-acid battery has a faster depletion of the active material and positive plates expansion, this phenomenon accelerates the aging problem, it can only provide 200 to 300 deep discharge/charge cycles. In addition, a lead-acid battery is not a proper candidate for fast charging, a full charge may take 14-16 hours (Battery University, 2019a). Lead-acid batteries are mostly used in ICE vehicles as 12V batteries to power accessories and start the engine. Due to its low cost, ease of replacement, and well-established interaction with the low-voltage accessories, lead-acid batteries are cost-effective for some automobile, forklifts, and standby applications.

Nickel-Metal Hydride Battery

Since early 20^{th} century, nickel-cadmium (NiCd) battery has been mostly applied

on portable devices with high cycle count, simple storage, various size, and performance options compared to a lead-acid battery. But in the 1990s, NiMH batteries with fewer toxicity problems and similar characteristics took over the share of NiCd. With new hydride alloys discovered, NiMH can provide 40% higher specific energy than that of an equivalent size NiCd, its energy density almost competes with Li-ion battery (Wikipedia, 2021). However, NiMH has two major drawbacks, it has a memory effect that causes capacity fade if not given a periodic full discharge cycle, and it ranks among the highest self-discharge in the class. The electric powertrain uses a modified hydride material to lower the self-discharge and alloy corrosion with robustness and long life span, but this leads to a sacrifice of specific energy (Battery University, 2019b). NiMH batteries have higher energy density than Lead-Acid batteries, and cheaper than Li-ion batteries, it is better used on HEV than a pure EV or plug-in hybrid electric vehicle (PHEV), where the energy density is less required.

Lithium-ion Battery

Lithium is the lightest chemical element and very active metal in the periodic table, thus rechargeable battery with lithium metal on the anode has great electrochemical potential and extraordinarily high energy density. In the mid-1980s, researchers discovered that cycling the battery with lithium metal resulted in dendrites on the anode which would penetrate the separator and cause an electrical short. In the late 20^{th} century, a shift to a non-metallic solution using lithium ions brought Li-ion battery to the most promising battery chemistry. Although it lowers the specific energy when compared with lithium metal battery, Li-ion battery provides a safe and higher voltage and current limits. Improvements in the active materials can further boost the energy density with a high cell voltage of 3.6V. In addition to high energy density,

Li-ion had the advantage of less maintenance, no memory effect, less self-discharge, simple pack design, with a flat discharge curve, it can release the stored energy in a flat voltage spectrum (Battery University, 2018b). The drawbacks of Li-ion batteries are obvious, abuse needs to be prevented by applying protection circuits, the cost to manufacture the batteries is relatively higher than other battery chemistries.

2.1.5 Battery Classification by Packaging Format

The battery material and chemistry play an important role in battery performance. However, the battery package format is also a key that battery engineers should consider. Different package format has a great influence on the overall module or pack performance in the end application, it has a direct connection with the system and structure design. In the EV field, there are three main package formats for the battery: cylindrical, prismatic, and pouch. The following schematics are three formats' construction of a Li-ion battery.

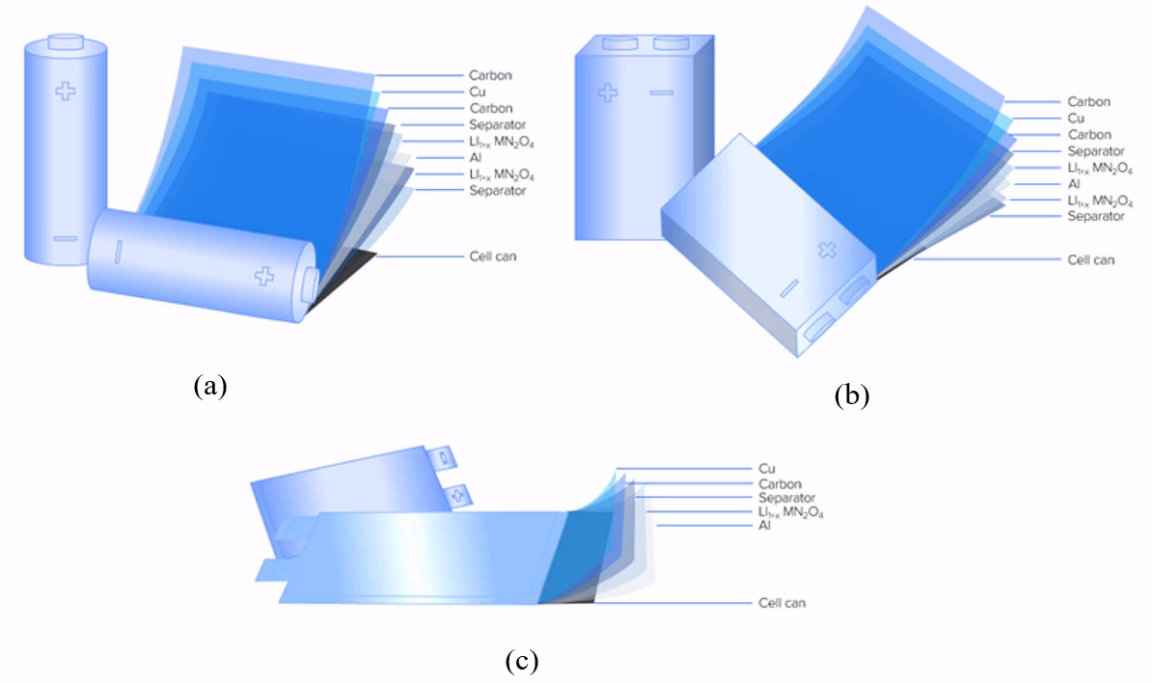

Figure 2.2: Three formats of a Li-ion battery: (a) cylindrical, (b) prismatic, (c) pouch (TWAICE, 2019)

Cylindrical Cell

The cylindrical cell is one of the most popular formats used for primary and secondary batteries. The cylindrical format is practically easy to be manufactured with good mechanical stability since this structure can sustain a relatively higher internal pressure. Many cylindrical cells have a positive thermal coefficient (PTC) switch as short circuit protection when the cell is exposed to a limit current. Some cylindrical cells also use pressure relief mechanisms like a membrane seal that will break when exposed to high pressure, and the charge interrupts device (CID) that inactivates the cell physically (Battery University, 2019c). Most cylindrical cells have high specific energy and good cycle performance with low cost, but this format rates low at packaging density.

Prismatic Cell

The prismatic cell is usually encased in aluminum or steel housing to sustain stability. There is no universal manufacturing design of the prismatic cell, some are jelly-rolled, and some are stacked by layers. Because of the firm housing for mechanical stability, it is often designed to allow some swelling due to gas buildup inside, and this distortion should be cared not to damage the battery compartment. The prismatic cell has high efficiency in packaging space but more cost for a manufacturer to produce, it is difficult to design the TMS and generally has a shorter cycle life than the cylindrical format (Battery University, 2019c).

Pouch Cell

Rather than using a metallic cylinder or housing, the pouch cell is sealed in a soft plastic aluminum bag with the conductive foil tabs welded to the electrodes. Without the metal enclosure, the pouch cell can achieve high energy density and has the most efficiency in space and packaging it also has good thermal conductivity for thermal design. However, this format is relatively vulnerable to damage, the battery compartment should consider support and allowance for the format under swelling due to gassing and avoid stacking with a sharp edge. Small pouch cells are popular to provide high load current for portable applications, and large cell is widely applied in an energy storage system with smaller cell quantity and simple pack design (Battery University, 2019c).

2.2 Battery Definitions

2.2.1 Battery Basics

Cell, Module, and Pack

HEVs and EVs have the battery pack as a final shape of the high voltage battery system. A battery pack is composed of many modules in series or parallel, and control systems like the battery management system, thermal management system. A module is generally many cells in series or parallel providing a frame avoiding shocks, vibration, and heat. A cell is the basic format of battery that is discharged or charged, it can be defined by functions as primary, secondary, or reserve, or by chemistries as lead-acid, nickel-metal hydride, Li-ion, etc., or by package formats as cylindrical, prismatic, pouch.

C- Rate and E- Rate

When describing a battery charge or discharge process, the current magnitude is often normalized against the battery capacity and is denoted by C-rate. A battery with a different nominal capacity has a different magnitude of current even with the same charging or discharging C-rate. For a 1C discharge, it means the battery will be discharged to empty in 1 hour, and it is 2 hours if discharged at 0.5C. For a battery with a nominal capacity of 50 Amp-hours, a 1C discharge current is 50 Amps, and a 0.5C discharge current has a magnitude of 25 Amps.

Another rate to describe charge or discharge is E-rate. When a battery is given with a nominal power, e.g., 500mWh, 1E rate discharge means the battery is discharged with 500mW power and drained in 1 hour. Similarly, 0.5E discharge rate indicates 250mW discharge power, and the battery will be drained in 2 hours.

2.2.2 Battery Technical Specifications

Nominal Voltage (V) – The average voltage when a cell is charged, it is determined by the chemical composition. Typically, a lead-acid battery applied on a vehicle is 12V, a Li-ion battery has a nominal voltage of around 3.6V.

Cut-off Voltage (V) – The minimum allowable operating voltage, this voltage defines the empty state of the battery.

Capacity or Nominal Capacity (Ah) – The total available Amp-hours when a battery is discharged under a certain C rate from 100% state-of-charge to the cut-off voltage. Capacity is calculated by multiplying the discharge current with the discharge time, it usually decreases with the increasing C rate (Team *et al.*, 2008).

Cycle Life – The charging-discharging cycle number when the battery reaches the minimum performance criteria. Cycle life is a function of temperature, DOD, C-rate, etc. A high DOD will decrease the cycle life.

Specific Energy (Wh/kg) – The nominal battery energy per unit mass, it is a characteristic of the battery chemistry and packaging. The specific energy determines the battery weight required for a given electric driving range.

Specific Power (W/kg) – The maximum available power per unit mass, it is a characteristic of the battery chemistry and packaging. The specific power determines the battery weight required for a given performance target. Vehicle acceleration is highly dependent on this factor.

Energy Density (Wh/L) – The nominal battery energy per unit volume, it is a characteristic of the battery chemistry and packaging. The energy density determines the battery size required for a given electric driving range.

Power Density (W/L) – The maximum available power per unit volume, it is a

characteristic of the battery chemistry and packaging. The power density determines the battery size required for a given performance target.

2.2.3 Battery Conditions

State of Charge (SOC) (%) – Equivalent to the fuel gauge in a conventional vehicle, the battery needs an indicator to represent the energy state. SOC is the battery current capacity as a percentage of the maximum capacity when it is fully charged. It is calculated by integrating current over the battery capacity over time.

Depth of Discharge (DOD) (%) – DOD indicates the discharged capacity of a battery, the equation holds: $DOD = 100 - SOC$. A deep discharge represents the battery is discharged to at least 80% DOD.

Terminal Voltage (V) – The voltage between the battery terminals when the load is applied to the battery. Terminal voltage is a function of SOC and charge/discharge current.

Open-circuit Voltage (OCV) (V) – The voltage between the battery terminals without load. OCV is a function of the battery SOC and temperature and is also affected by battery aging. OCV curve is often used to predict SOC, or as a diagnosis of battery state of health (Lei and Han, 2019).

Internal Resistance – The resistance within the battery, it is a function of SOC and charge/discharge condition. An increasing internal resistance decreases the battery efficiency, more heat is converted from the charging energy, which results in thermal instability.

State of Health (SOH) (%) – SOH is an indicator of the battery aging condition compared to its ideal condition. A 100% SOH stands for a battery produced from the

manufacture and meets the specification. The battery capacity, internal resistance, and self-discharge are indicators of SOH. SOH is commonly not provided by the manufacture, and it decreases over time and use.

2.3 Battery Management System

2.3.1 Battery Management System Overview

The battery management system (BMS) is applied to provide battery safety and prolonged life span, give the user the state-of-function including SOC and SOH, remind the user of any caution or necessary service, and indicate the end-of-life when the battery capacity reaches the target. In particular, BMS is required to protect the battery and offer accurate SOC estimation.

Unlike the liquid fuel which has a physical dimension to measure, it is a challenge for BMS to predict the SOC of an electrochemical storage system. The readout of SOC is inaccurate without considering the battery capacity fade since each charge/discharge causes a loss of the factory capacity. Capacity is a primary indicator of battery SOH, and its estimation is a major part of BMS. However, the capacity fade is difficult to estimate due to that the voltage and internal resistance are imperceptibly affected by aging. The capacity fade from 100% to 70% is notable, even the capacity drops to 50%, the battery can still sustain some operation. But a low capacity may lead to many anomalies including inaccurate SOC estimation, voltage differences causing cell imbalances, drastic internal resistance rise (Battery University, 2019d).

The BMS plays a great role in protecting the battery when charging and discharging, it disconnects the battery when the limit condition is reached. Some BMS standards have been established such as system management bus (SMBus) for portable applications, and controller area network (CAN) bus, local interconnect network (LIN) bus for automotive application. The basic of these systems is monitoring the individual cell voltage. Some advanced systems are also able to measure the temperature and current of the cells (Battery University, 2019d).

2.3.2 Battery Modeling

BMS plays an important role in monitoring and controlling the battery pack of a hybrid and EV, the main function of a BMS includes an accurate SOC and SOH estimation, battery voltage, current, temperature measurements. Since some of these parameters cannot be measured directly with an on-board vehicle control system, a high-fidelity battery model is required. While the accuracy of a battery model is desired, its complexity cannot be excessive so that it is not feasible on a real-time BMS application. When conducting the battery modeling, the designer is confronted with a trade-off between the model accuracy and computation effort. Many researchers have investigated various battery models, they are mainly identified into the following categories: (i) equivalent circuit model, (ii) empirical model, (iii) electrochemical model.

Equivalent Circuit Model

The equivalent circuit model (ECM) uses an equivalent circuit containing an OCV source, internal resistance, and RC circuits to simulate the circuit characteristics of the battery to determine the terminal voltage. It gains popularity due to low

computational cost and successful simulation of all battery performances. This model reduces electrochemical applications and only requires a few parameters that can be easily obtained in experiments to achieve high-fidelity battery predictions.

A typical ECM with one RC branch is shown in Figure 2.3. It consists of three major parts: a static part as the voltage source indicates the thermodynamic properties of the battery chemistry like the nominal capacity and OCV as a function of SOC; a dynamic part with a parallel-connected resistor and capacitor as the RC branch represents the kinetic performance such as internal impedance and overvoltage; and a source or load with the terminal voltage completes the circuit for charge or discharge regimes (Liaw *et al.*, 2004).

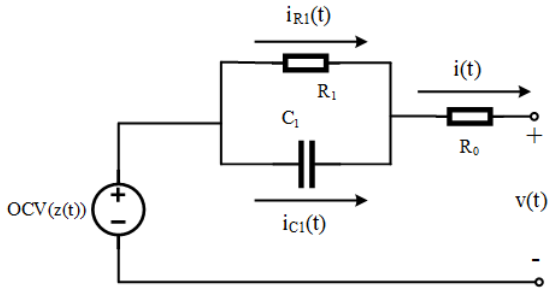

Figure 2.3: Equivalent circuit model schematic

Increasing the number of RC branches produces a higher-order ECM that can capture more dynamics of the battery, but the computation cost goes up accordingly. In addition, a hysteresis state can be incorporated into the terminal voltage estimation to model the battery hysteresis behavior during charging and discharging (Hu *et al.*, 2012; Ahmed, 2014). Table 2.1 presents the terminal voltage equations for the first, second, third-order ECM with a hysteresis factor, where h_k is the hysteresis, OCV is a function of SOC as a notation of z.

Table 2.1: First, second, third order ECM equations with hysteresis

Model	Terminal Voltage Equation
First-order ECM	$V_T = OCV(z) - R_0 i - R_1 i_{R_1} + h_k$
Second-order ECM	$V_T = OCV(z) - R_0 i - R_1 i_{R_1} - R_2 i_{R_2} + h_k$
Third-order ECM	$V_T = OCV(z) - R_0 i - R_1 i_{R_1} - R_2 i_{R_2} - R_3 i_{R_3} + h_k$

Empirical Model

Empirical models are often considered as simplified electrochemical models with the essential nonlinear characteristics of the battery. The terminal voltage is represented as a mathematical function such as a reduced order polynomial (Meng *et al.*, 2018). Similar to ECM, the empirical model can be implemented readily with few efforts on parameter identification.

There are three classical empirical models in the literature: the Shepherd model (Moore and Eshani, 1996), the Unnewehr universal model (Unnewehr and Nasar, 1982), and the Nernst model (Plett, 2004). The equations of these three models are listed in Table 2.2, where R_0 is the internal resistance, E_0 is the initial cell voltage, K_1, K_2, K_3, K_4 are the polarization resistance, these parameters can be easily identified by experiment.

Table 2.2: Typical empirical models

Model	Terminal Voltage Equation
Shepherd Model	$V_T = E_0 + R_0 i + \frac{K_1}{SOC}$
Unnewehr Universal Model	$V_T = E_0 + R_0 i + K_2 SOC$
Nernst Model	$V_T = E_0 + R_0 i + K_3 \ln(SOC) + K_4 \ln(1 - SOC)$

In (Hussein and Batarseh, 2011), the author conducted research on these three

models and compared the accuracy of terminal voltage and SOC estimation. The result shows that the Shepherd model has better performance under the continuous current test, and the Nernst model shows the best overall performance with more parameters and correction factors. As a rule of thumb, a combined model based on the aforementioned three empirical models can provide a more accurate estimation (Plett, 2004). The terminal voltage equation is as follows:

$$V_T = E_0 + R_0 i + \frac{K_1}{SOC} + K_2 SOC + K_3 \ln(SOC) + K_4 \ln(1 - SOC) \tag{2.1}$$

Electrochemical Model

The electrochemical model is established to describe the inner chemical and physical reactions of the battery. Many physical laws are derived from the electrochemical model, such as Faraday's first law, Ohm's law, Fick's law of diffusion, and the Butler-Volmer equation (Meng *et al.*, 2018). The electrochemical model is generally complex with partial differential equations to express lithium diffusion inside the electrodes and electrolyte, and it requires numerous parameters like diffusion coefficients and electrode physical dimensions that add up the computation cost. However, the electrochemical model is still a better candidate to model the physical phenomenon in the battery to predict battery SOC and SOH. In most cases, model reduction is carried out to reduce the computation cost and makes it possible to be implemented on real-time application (Ahmed, 2014).

In (Smith and Wang, 2006b), the authors built a 1D electrochemical model based on the processes inside a Li-ion cell. The mathematical expressions that govern the charge and species conservation are given by solid and electrolyte phases. The

electrolyte phase of the charge is given:

$$\frac{\partial}{\partial x}(\kappa^{eff}\frac{\partial}{\partial x}\phi_e) + \frac{\partial}{\partial x}(\kappa_D^{eff}\frac{\partial}{\partial x}\ln c_e) + j^{Li} = 0 \tag{2.2}$$

where the boundary condition is:

$$\frac{\partial \phi_e}{\partial x}|_{x=0} = \frac{\partial \phi_e}{\partial x}|_{x=L} = 0 \tag{2.3}$$

The solid phase of the charge is given:

$$\frac{\partial}{\partial x}(\sigma^{eff}\frac{\partial}{\partial x}\phi_s) - j^{Li} = 0 \tag{2.4}$$

where the boundary condition is:

$$\begin{aligned} -\sigma_-^{eff}\frac{\partial \phi_s}{\partial x}|_{x=0} &= \sigma_+^{eff}\frac{\partial \phi_s}{\partial x}|_{x=L_-+L_{sep}+L_+} = \frac{I}{A}, \\ \frac{\partial \phi_s}{\partial x}|_{x=L_-} &= \frac{\partial \phi_s}{\partial x}|_{x=L_-+L_{sep}} = 0 \end{aligned} \tag{2.5}$$

The electrolyte phase of the species is given:

$$\frac{\partial(\varepsilon_e c_e)}{\partial t} = \frac{\partial}{\partial x}(D_e^{eff}\frac{\partial}{\partial x}c_e) + \frac{1-t_+^0}{F}j^{Li} \tag{2.6}$$

where the boundary condition is:

$$\frac{\partial c_e}{\partial x}|_{x=0} = \frac{\partial c_e}{\partial x}|_{x=L} = 0 \tag{2.7}$$

The solid phase of the species is given:

$$\frac{\partial c_s}{\partial t} = \frac{D_s}{r^2}\frac{\partial}{\partial r}(r^2\frac{\partial c_s}{\partial r}) \tag{2.8}$$

where the boundary condition is:

$$\frac{\partial c_s}{\partial r}|_{r=0} = 0, D_s \frac{\partial c_s}{\partial r}|_{r=R_s} = -\frac{j^{Li}}{a_s F} \tag{2.9}$$

Ohm's law, i.e., Equation 2.2 and Equation 2.4, calculate the liquid electrolyte and solid electrode potentials. Equation 2.6 and Equation 2.8 are the Fick's law of diffusion to obtain solid-state and liquid-state transport of Li. The authors discretized the 1D macroscopic domain into dozens of control volumes to get the numerical solution. The field variables: lithium concentration in electrolyte phase c_e, lithium concentration in solid phase at electrode/electrolyte interface $c_{s,e}$, volume-averaged electrical potential in electrolyte phase ϕ_e, and in solid phase ϕ_s, are solved with current as input. The cell terminal voltage is calculated:

$$V_T = \phi_s|_{x=L} - \phi_s|_{x=0} - \frac{R_f}{A} I \tag{2.10}$$

where R_f is the contact resistance between current collectors and electrodes.

2.3.3 Battery State Estimation - Coulomb Counting

The Coulomb counting method is the most common way to estimate the battery SOC. The nominal capacity of a battery can be regarded as a constant, the SOC can be calculated as an integral of current on a time domain. Many battery management systems calculate SOC using this method or its enhancement. In these approaches, the current entering and leaving the battery is multiplied by time, and the SOC is estimated by subtracting (discharge) or adding (charging) the cumulative

net charge (Zhao *et al.*, 2016):

$$SOC(t) = SOC(t_0) - \frac{1}{C_{nom}} \int_{t_0}^{t} \eta \cdot I(t) dt \tag{2.11}$$

where C_{nom} is the nominal capacity obtained from the manufacturer or laboratory experiment. $SOC(t_0)$ is the SOC at the initial stage, which can be estimated by mapping with OCV or the extended Kalman filter based approach (Xing *et al.*, 2014). η is the coulombic efficiency which is a function of charge and discharge condition, temperature, SOH, and battery chemistry. I(t) is the current that is positive at discharging and negative at charging.

The coulomb counting based on time-domain is simple to be implemented to all battery chemistries. However, due to integration over time, the error caused by sensor noise and inaccuracies will accumulate, thus regular calibration is required. An accurate initial SOC is also very important to achieve high accuracy. When implemented on a real-time application, a complete charge and discharge are commonly conducted to perform the calibration.

Chapter 3

A Review of Battery Ultra-Fast Charing and Thermal Management System

3.1 State of Art of Electric Vehicle Battery Ultra-Fast Charging

While the automotive manufacturers are putting great effort to improve the covering range and life span of EVs, the acceptance of pure EVs by consumers is still limited. Due to the low energy density compared with gasoline fuel, EV battery is overshadowed by ICE because of range anxiety and much longer charging time. A gasoline vehicle can refuel a 50-liter tank that holds a calorific value of 600kWh in several minutes, while it would be more than ten hours for an EV to charge the battery pack with 100kWh of energy. To address the gap in charging time, ultra-fast charging

capability has been a key feature of the EV battery.

3.1.1 Fast Charging Infrastructure

Either alternating current (AC) or direct current (DC) can be applied to charge an EV, and DC is preferred by the EV industry due to a much higher charging speed. Early in 2011, the Society of Automotive Engineers (SAE) proposed three DC charging levels starting from a 36kW charger that is able to charge an EV from 20% SOC to 80% SOC in 1.2 hours, to the highest charging level with 240kW power charger that can charge the EV from empty to 80% SOC within 10 mins (Pokrzywa, 2011). Since then, automotive manufacturers have been making progress in increasing the EV chargers' power. There are three common DC fast charging posts that provide a charging power of over 50kW: CHArge de MOve (CHAdeMO), Combined Charging System (CCS), and GB/T standard connectors. CHAdeMO standard was established by the partnership of Toyota, Nissan and Mitsubishi, a Nissan LEAF is able to be charged from empty to 80% SOC in around half an hour (Verma *et al.*, 2020). Tesla firstly introduced 120kW charging posts with custom connectors, followed by CCS standard, 150kW chargers were developed (Tomaszewska *et al.*, 2019). In 2017, Porsche developed an ultra-rapid charger rated at 350kW by combining two CCS charging posts. The first light-duty EV with this charger built by Porsche, the Taycan, debuted in 2019.

However, the increasing power capability of the EV charger does not translate directly to faster charging, the actual charging power is normally lower than the rated power of the charger under continuous operation and varies with the EV specifications

and environmental conditions. Particularly, the charging speed is greatly reduced under a low ambient temperature. In fact, the high-power fast charging part is only achieved before 80% SOC, the battery is then charged by a constant voltage. This standard constant current – constant voltage and commonly used fast charging protocol for Li-ion batteries tend to decrease the polarization losses and risk of overheating at high SOC range (Mussa *et al.*, 2017).

3.1.2 Degradation Mechanisms

Similar to the organ of a living body, the EV battery aging is the result of the operation and the environmental conditions, e.g., charging or discharging SOC level, charging speed, and temperature. While ultra-fast charging can bring much convenience for EV usage, a high C rate charging usually increases the battery impedance and narrows the capacity window in a long term. With respect to analyzing the effect of ultra-fast charging, three degradation mechanisms by the physical material dynamics are generally considered (Schindler *et al.*, 2018).

Lithium Plating

For a Li-ion battery, metallic lithium tends to accumulate at the negative electrode during a low-temperature charging, high SOC range, and large current operations. Due to a large polarization force by the great potential difference between the electrolyte and the solid negative electrode, lithium ions at the interface of electrode and electrolyte deposits on the surface of the anode instead of intercalating back in the anode particles (Hein and Latz, 2016). This process, lithium plating, results in a large amount of cyclable lithium loss, thus reducing the durability and electrochemical cycling ability of the battery and causing safety hazard in the long run. As for the

solutions to this phenomenon, active control can be taken to design a proper charging protocol by associating the charging current magnitude with battery SOC and manage to charge at an appropriate temperature range. Furthermore, an excessive anode particle capacity is often considered a passive control.

Electrolyte Decomposition

Electrolyte decomposition most likely happens when the electrochemical potential of an electrolyte system reaches the limit of instability, thus a surface film would deposit on both positive and negative electrodes. Even worse, this unstable reaction may generate gaseous products (Vetter *et al.*, 2005). An increasing temperature is a major cause to aggravate the unstable system and accelerate electrolyte decomposition. To avoid the decomposition reaction, the charging protocol should maintain the electrolyte potentials within a proper range. Meanwhile, optimized temperature control plays a crucial role in slowing down electrolyte decomposition.

Particle Cracking/Transition Metal Dissolution

As the battery ages, the active materials of the battery would experience a mechanical disintegration, thus the intercalation reaction is influenced by the loss of surface elements. This phenomenon is worse by the dissolution of the metal oxide in practical electrolytes when the battery consists of Manganese spinel or has a layered structure. The cracking particles or transition metals may spread through the cell separator and have a reaction with the materials of the anodic SEI. Moreover, the products of the reaction would accelerate the reduction of SEI since the protective effect is broken. Particle cracking and transition metal dissolution usually occur at high SOC and high potentials, they can be minimized by the selection of the active materials and avoiding high cycling rates at high SOC range. In addition, this

degradation mechanism is activated and accelerated by a high temperature, a proper temperature control can mostly circumvent the negative effects (Wohlfahrt-Mehrens *et al.*, 2004).

3.2 State of Art of Battery Thermal Management System

Prior sections explained some major degradation mechanisms from physical and chemical points of view within the battery. These mechanisms describe how the battery is aged, and ultra-fast charging could aggravate the phenomenon or even cause failure. The conclusions of how to minimize the aging effects by ultra-fast charging were drawn in two directions. Many researchers investigated the first way to optimize the fast charging protocol by the combination of different charging modes, e.g., applying DC or AC, multistage constant current, or pulse current to the battery at different SOC range. This is because that the degradation mechanisms are sensitive to the electrical potential and current magnitude. The other factor that the degradation mechanisms are closely correlated with is the temperature. Therefore, a battery TMS is critical to maintaining a desired temperature range under complicated operation conditions and extreme ambient conditions. When the battery is charged or discharged by a large current magnitude under fast charging or intense driving, a large amount of heat is usually generated from the battery, this heat should be dissipated effectively to avoid unexpected temperature rises. While the vehicle is in the northern area or winter under -10°C, the battery TMS should be able to keep a mild temperature as the power and energy of a battery are excessively reduced, therefore, limiting the driving range

or performance under extremely low temperature (Zhang *et al.*, 2002). In terms of a battery pack, the battery TMS should ensure an even temperature distribution across the battery modules, an uneven temperature distribution may lead to cell balance issues and circumscribe vehicle performance. Typically, most of the batteries achieve the best performance and life between 25 to 40°C, and the temperature distribution between battery modules should be less than 5°C (Pesaran, 2002). As for an EV application, the battery TMS should also consider the cost, compactness, reliability, parasitic power consumption, etc.

In most cases, the cooling effect of a battery TMS is the key performance indicator since temperature rise by the battery heat generation is significant. Even though operating under low ambient temperature requires the battery TMS to provide heat, some changes can be made for the cooling system to heat the battery inversely. In this work, the cooling effect of a battery TMS will be most considered. There are many methods to classify battery cooling systems such as by medium, by energy source, and by contact. First, also mostly referred to, a battery cooling system is divided into air cooling, liquid cooling, or phase change materials (PCM) cooling by the physical state of the cooling medium. Second, depends on the energy source, passive cooling only takes energy from the ambient environment, while active cooling consumes energy from the vehicle energy unit. Lastly, with the cooling medium in contact with the batteries or not, the cooling system is categorized by direct cooling and indirect cooling. In the following sections, the cooling systems with different mediums will be reviewed, and some industrial examples will be provided.

3.2.1 Air Cooling Method

Using air to cool the battery pack may be the simplest approach, air cooling system has the advantages of potential savings in parasitic power consumption and weight. Heat transfer of an air cooling system is achieved by blowing the air across the battery modules, several schematics are shown in Figure 3.1 (Pesaran, 2001). It is obviously invalid to cool the battery by natural air convection, therefore, one or more fans are required to blow the airflow. Passive cooling is simply blowing outside air through the battery pack as Figure 3.1A, but this layout cannot be practically applied as it is impossible to heat the battery pack at low temperature. Generally, the outside air passes through the vehicle heater and evaporator cores before blowing the battery pack to reach the desired temperature as shown in Figure 3.1B, and the preconditioned cabin air can join in the airflow as a closed-loop temperature control. Furthermore, as indicated in Figure 3.1C, the air can be partially circulated in the loop and conditioned by auxiliary or vehicle heater and evaporator cores for enhanced active temperature control. As a typical industrial example for this air cooling system, the Toyota Prius supplies the cabin air to cool the battery pack in Figure 3.2.

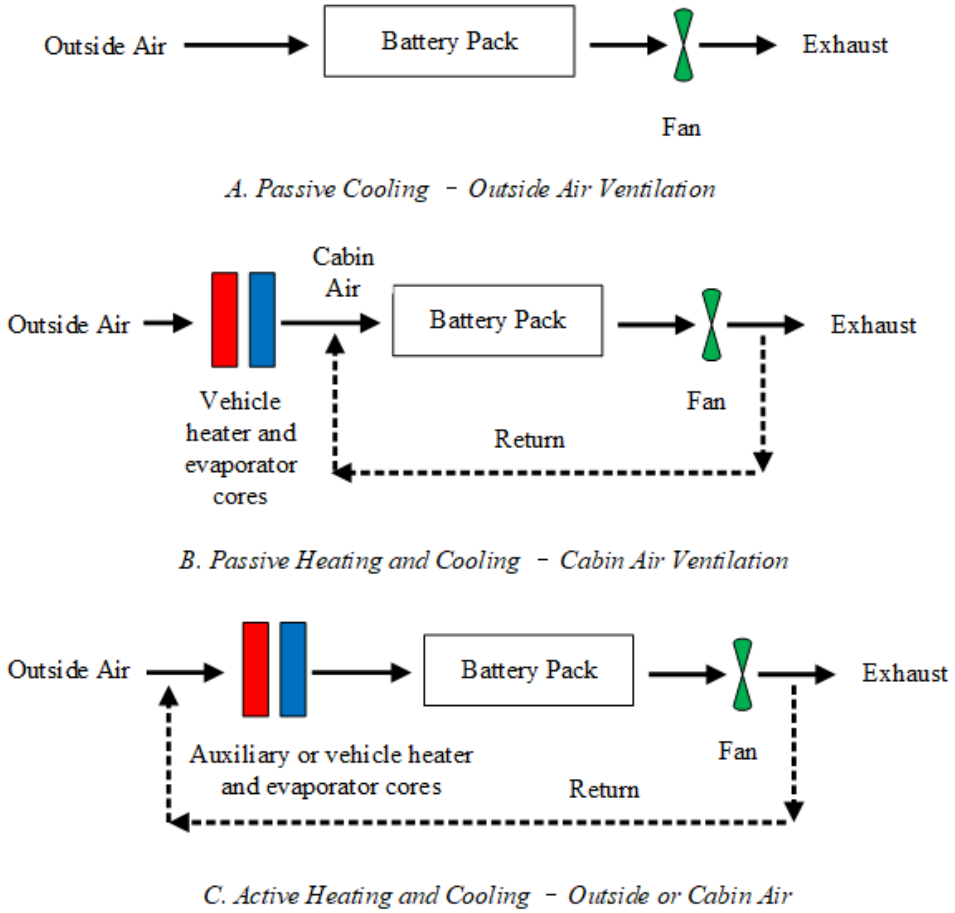

Figure 3.1: General schematics of air cooling method (Pesaran, 2001)

However, the air cooling method cannot provide the battery pack with uniform temperature control. Even with an optimized layout with parallel and series vents, the temperature difference between modules is hard to be controlled under 5°C. Furthermore, if the ambient temperature is too high (above 40°C), and the battery is under a stressful condition with a high operating temperature, it is impossible for the air cooling method to cool down the battery under 40°C. When applying to a high-power density battery pack, air cooling systems usually become prohibitively large, thus limiting the feasibility on commercial vehicles (Giuliano *et al.*, 2012).

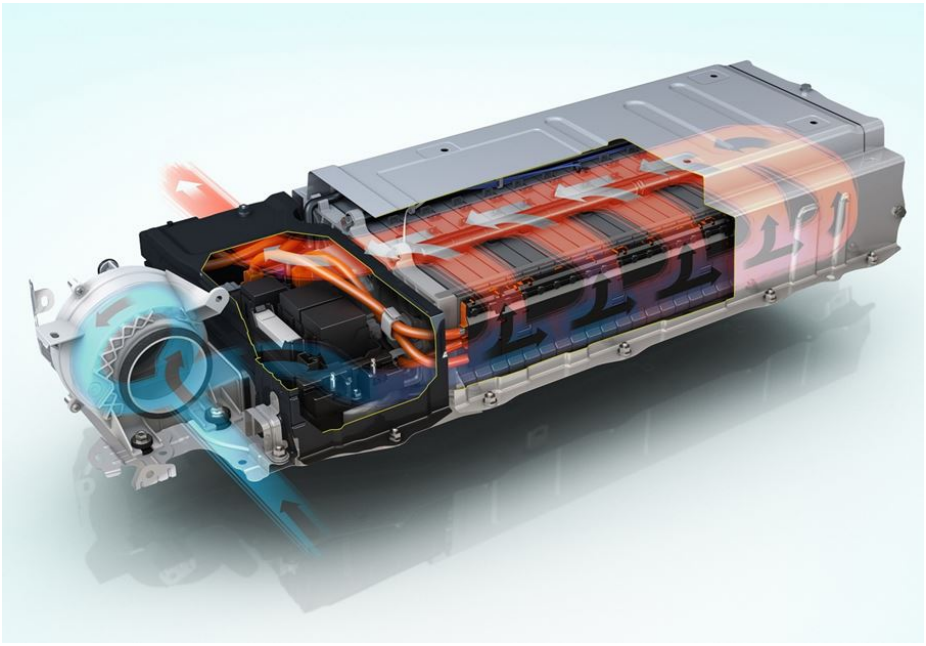

Figure 3.2: Air cooling battery thermal management system for the Toyota Prius (Synergy Files, 2018)

3.2.2 Liquid Cooling Method

As an air cooling system is not effective to dissipate heat for a large-scale battery under abuse conditions, a battery TMS using liquid could be more competent to remove a large amount of heat by circulating coolant through discrete tubing or water jackets around battery modules; directly submerging modules in a dielectric fluid; or placing heated/cooled plates as heat sinks between the battery modules or cells (Pesaran, 2001). A liquid cooling battery TMS generally uses water, glycol, oil, or even refrigerants as the heat transfer medium (Rao and Wang, 2011). Three typical schematics of liquid cooling systems are shown in Figure 3.3 (Pesaran, 2001). The liquid coolant is circulated by a pump, the heat is transferred by a heat exchanger. Passive cooling only utilizes outside air to remove the heat from the coolant in the heat exchanger, while active cooling uses liquid in the heat exchanger for improved

efficiency. If more heat from the battery needs to be removed or the battery needs to be heated, an airconditioned heat exchanger is applied to transfer the heat from the coolant to the refrigerant from the condenser or transfer the heat from the air of the evaporator to the coolant.

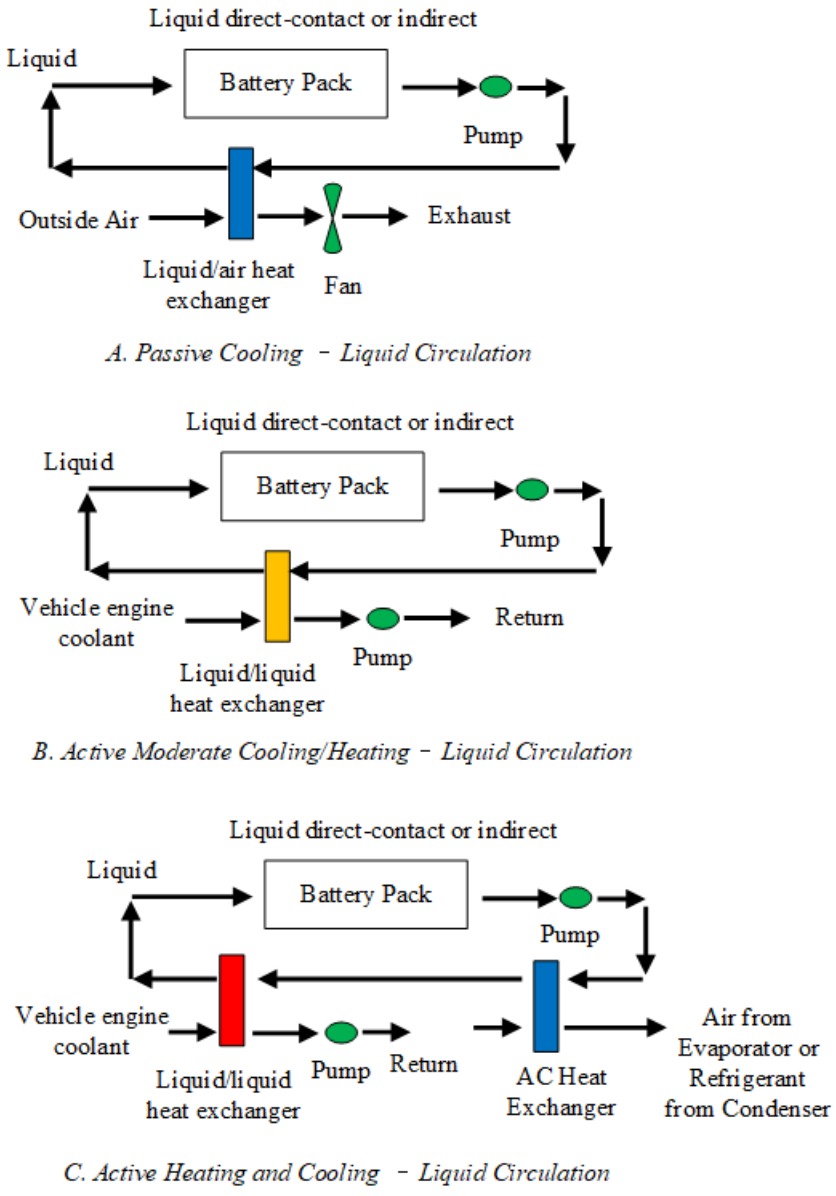

Figure 3.3: General schematics of liquid cooling method (Pesaran, 2001)

Many researchers have put the effort into developing liquid cooling systems for batteries by FEA thermal modeling. In (Ye *et al.*, 2019), two cooling plates were placed in a module consisting of LFP batteries, orthogonal experimental design method was carried out on the thermal model to optimize the geometry of the battery module and the cooling plates. The conclusion was drawn that an optimized geometry of the cooling system could evidently reduce the battery temperature rise and the pressure drop of the coolant. Panchal, S. et al. (Panchal *et al.*, 2015) performed an experiment to observe the temperature distribution and the heat generation of a 20Ah Li-ion pouch cell with dual liquid cooling cold plates, different C-rate discharge tests of 1C, 2C, 3C, 4C were conducted under different boundary conditions with cooling bath temperature of 5°C, 15°C, 25°C, and 35°C.

Compared with air cooling, liquid cooling has higher thermal conductivity, better cooling efficiency, and uniform temperature distribution control, it also occupies less volume and is able to achieve both heating and cooling. Whereas sealing of the coolant channels adds complexity to the liquid cooling system, the cooling system also increases a great amount of weight to the vehicle and production cost. Nowadays, liquid cooling methods, as the best option for attaining a sufficiently energy-dense pack without too large of a temperature rise, are widely applied to mass-produced automobiles. Several industrial examples applied with the liquid cooling method are presented as follows. It is noticeable that the layout of the cold plates as heat sinks makes a great difference in the efficiency of heat dissipation, the configurations can be generally classified into two types depending on the position of the heat sinks. Audi Q8 concept applies the heat sinks on the bottom surface of the battery modules or pack, it is named as edge cooling method. While Tesla Model S and Chevy Volt

have the heat sinks embedded between the cells, this layout is named as an inter-cell cooling method.

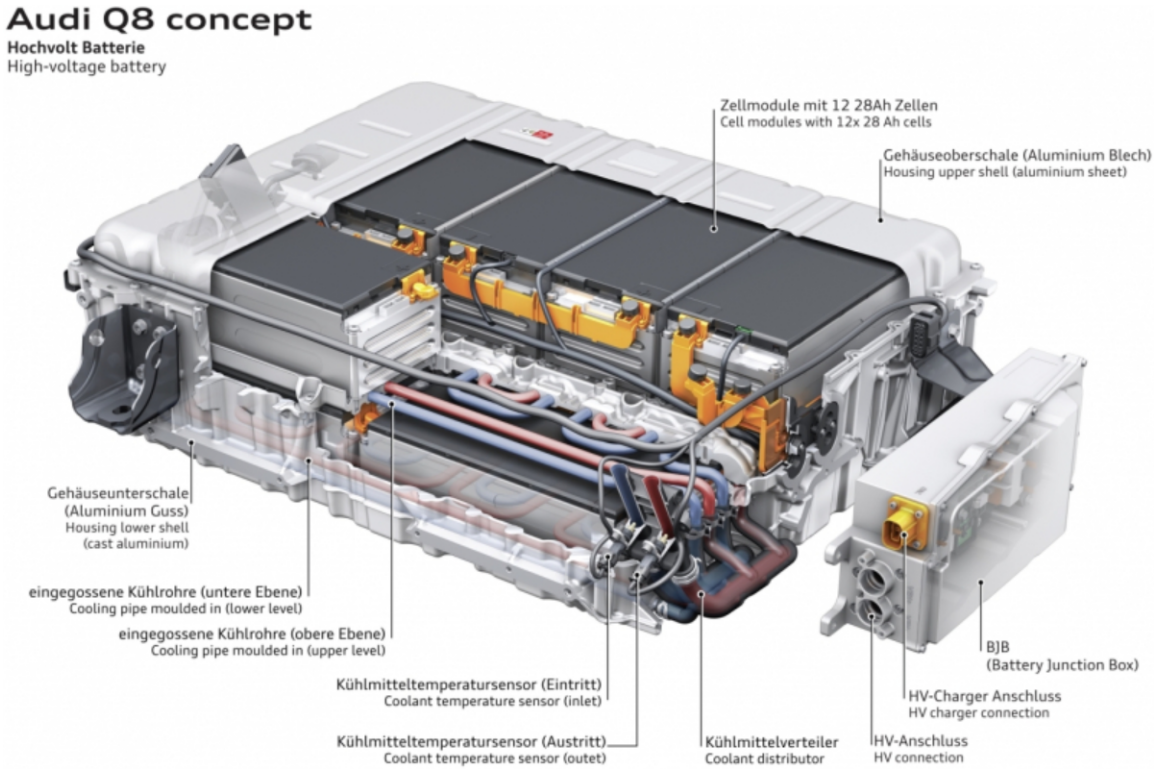

Figure 3.4: Audi Q8 concept battery pack with edge liquid cooling method (Green Car Congress, 2017)

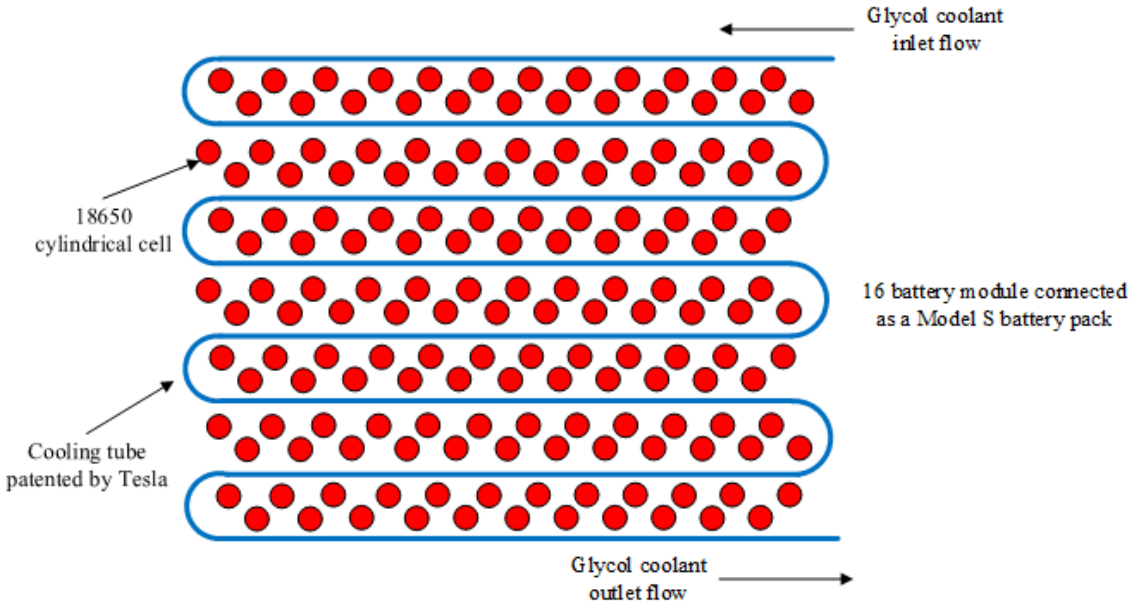

Figure 3.5: Tesla Model S battery pack schematic with inter-cell liquid cooling method (Bower, 2015)

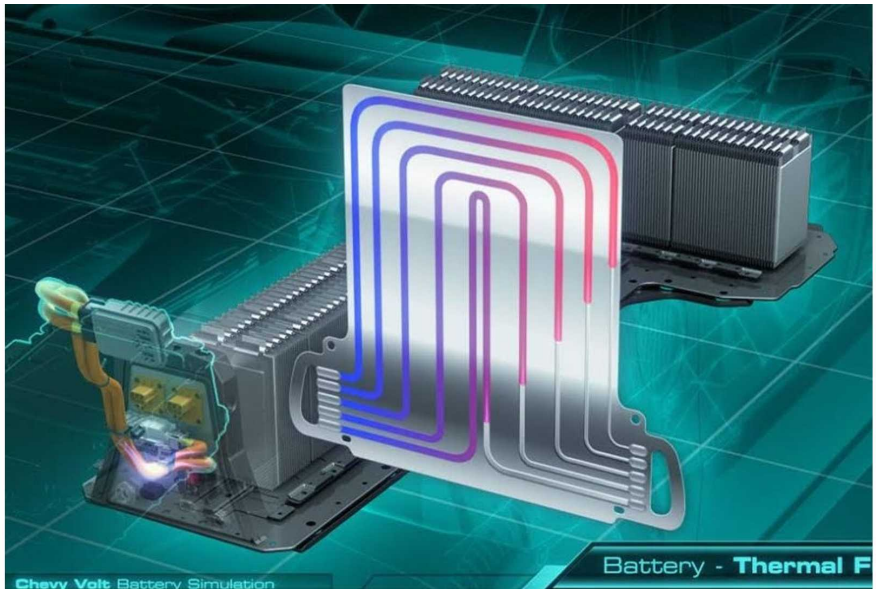

Figure 3.6: Chevy Volt battery pack schematic with inter-cell cooling method (Bower, 2015)

3.2.3 Phase Change Materials Cooling Method

The phase change process is isothermal, which is the most important characteristic of PCM as its melting point can be used to maintain a desired operating temperature range and uniformity across the cells in EVs and HEVs application (Malik *et al.*, 2016). A general schematic of the battery TMS applied with PCM is shown in Figure 3.7. The cells of the battery pack are usually immersed in the PCM so that all the generated heat by the batteries is absorbed by the PCM. The generated heat leads to the temperature rise of the batteries and the PCM. As the temperature of the bulk increases to the melting point of the PCM, the material will change phase and maintain its temperature when absorbing more heat from the batteries. However, a large amount of heat in the PCM still needs to be removed. It will consume the energy from the batteries significantly if the heat dissipation by a refrigeration system is completely driven by the battery pack, therefore, the schematic in Figure 3.7 provides a possible solution with an external PCM tank. The PCM tank is attached to the battery cooling system which circulates the hot PCM, and the heat in the tank is transferred to the ambient environment by convection. This solution can greatly reduce the load of the battery cooling system that saves the battery energy for more driving range.

There are many types of research on PCM both in the experiment or numerical simulation, but there are few industrial examples applying the PCM cooling method. Jaguemont, J. et al. in (Jaguemont *et al.*, 2018) gave an elaborated review of passive cooling/heating systems for batteries, discussed the thermal properties of organic, inorganic, and eutectic PCM. The PCM in thermal systems is modeled in both the enthalpy method and the temperature method. Much literature about passive TMS

with PCM was reviewed, some experimental results were summarized. Hybrid solutions combining PCM with air or liquid cooling methods were also investigated to ensure improved performance. In (Khateeb *et al.*, 2004), Khateeb et al. designed an electric scooter with PCM battery TMS. A comparative study of the PCM with aluminum foam and aluminum fins was conducted to improve the low thermal conductivity and natural convection. They also performed an experimental validation in (Khateeb *et al.*, 2005) and concluded that a PCM cooling method with aluminum foam could offer 50% reduction of the battery temperature rise compared with the case of natural convection cooling. The PCM cooling method can provide a compact, inexpensive battery TMS with less parasitic power needed to pump air or liquid coolant. The major disadvantages of PCM though are inefficient heat transfer due to poor thermal conductivity, high initial costs and adding weight to the vehicle, and volume expansion during melting (Malik *et al.*, 2016; Khateeb *et al.*, 2004).

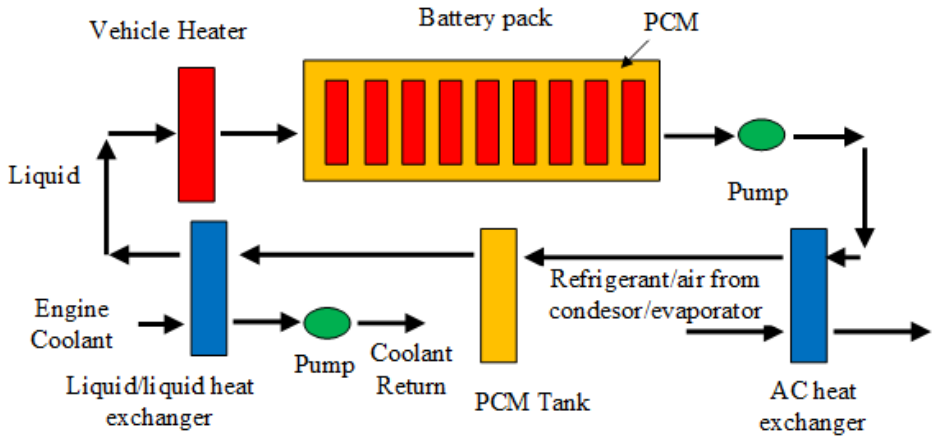

Figure 3.7: General schematic of PCM cooling method (Malik *et al.*, 2016)

Chapter 4

Experimental Comparison between Edge Cooling and Inter-Cell Cooling Battery Modules

4.1 Introduction

For ultrafast charging applications, where vehicle battery packs are charged in as little as ten minutes, a large amount of heat is generated by the cells. A fast-response and effective TMS is required to maintain the battery within an acceptable temperature range. Nowadays, automobile manufacturers are widely applying liquid cooling methods to the battery TMS due to their high efficiency. Whereas the configuration of a liquid cooling system makes a great difference in the battery temperature control. Generally, there are two types of liquid cooling configurations that are frequently put into production.

The first configuration is edge cooling, where a thermally conductive plate, typically aluminum, is placed between the cells. The thickness of the plate can be designed according to the cell type, generated loss, and desired temperature rise (He *et al.*, 2018; He, 2018). A liquid cooling plate on the edge of the battery module draws heat from the plates between the cells. This method is cost-effective, fairly easy to implement, and is commonly used in EV battery packs. Large liquid cooling plates are typically placed on the bottom of the pack with modules set on top and cooled from one side. Typical industrial examples were the Audi Q8 concept shown in Chapter 3 that applies with one edge cooling plate at the bottom, and the Chrysler Pacifica Hybrid that has two cooling plates on two sides of the batteries.

The second configuration of the liquid cooling systems is inter-cell cooling, where a liquid cooling plate is placed directly between the cells. This method is much more effective at removing heat since the path from the cell to the liquid coolant is short. It is more complex and expensive though since many more cooling plates are necessary and the plates must be very thin to minimize pack mass and volume. Chevy Volt is a representative of the inter-cell cooling method, the cooling schematic was presented in Chapter 3. Another example is Tesla Model S, though it utilizes small format 18650 cylindrical cells, a ribbon-like coolant channel snakes through the battery cells to improve the heat sink contact with the cells (Easy Electric Cars, 2019).

By directly comparing edge cooling and inter-cell cooling, this chapter aims to provide insight into the effectiveness of both methods for ultrafast charging applications. A set of tests are designed and performed on two prototype modules, and several results are presented including temperature rise for charging rates of up to

5C, where a battery is charged to 80% SOC in about ten minutes. The thermal conductivity of modules is also measured, and temperature is measured for a series of repeated fast charges and drive cycles which emulate real-world use of the modules.

4.2 Experimental Apparatus and Module Design

The prototype liquid-cooled modules are designed for a Kokam NMC 31 Ah cell. Each module has three cells connected in parallel, and an environmental chamber and a chiller are used to maintain the desired test temperature. This section outlines the battery specification, module design, and test equipment.

4.2.1 Cell and Thermal Pad Specifications

A Kokam SLPB78216216H pouch cell is used which is capable of high C-rates without compromising safety or cycle life (Kokam, 2016). More detailed specifications are listed in Table 4.1, where the nominal resistance and power density are calculated at 50% SOC and $20°C$ from hybrid pulse power characterization (HPPC) test data. To allow the pouch cell to expand during cycling and to improve the thermal interface between the cell and cooling plates, the modules are designed with a layer of compressed thermally conductive foam (Laird Technologies® TflexTM HR440, 1.8 W/mK) that provides uniform pressure over the surface of the cell.

Table 4.1: Testing cell specification

Manufacturer	Kokam	Nominal Resistance (mΩ)	0.9
Model	SLPB78216216H	Mass (g)	720
Chemistry	NMC	Power Density (kW/kg)	1.7
Capacity (Ah)	31	Voltage Limit (V)	2.7 - 4.2
Dimension (mm)	226×227×7.8		

4.2.2 Edge Cooling Module Design

The developed prototype edge cooling module aims to emulate designs that would be used for a commercial application, while still being practical to design and build. Structurally, the module must compress the cells and provide even pressure of around 8 PSI over their surface to ensure the cells do not expand and delaminate during cycling. The module must also have excellent thermal connections between the cell, plates between the cells, and cooling plates on the edges of the cells. The prototype module, as shown in Figure 4.1, compresses the cells between two large plastic plates and uses a series of components with machined flat surfaces, thermal grease, and thermal pads on the cell surfaces to ensure heat is transferred to the liquid cooling plates as effectively as possible. Figure 4.2 is the schematic of the heat flow in the edge cooling module as a half of the Computer-aided design (CAD) drawing. A design more suitable for mass manufacture would typically make design compromises that add thermal resistance to the module, so the results here represent the best case.

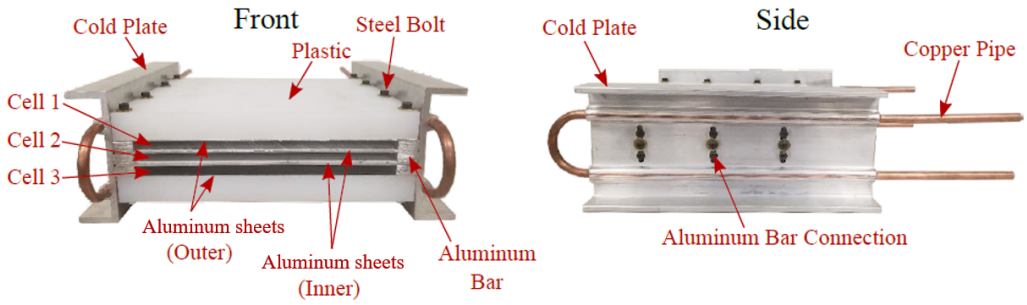

Figure 4.1: Configuration of the edge cooling module

The cells are sandwiched between four aluminum plates. The two outer plates are half the thickness of the 2 mm thick inner plates since they only have one contact face with the cell. A one-inch-thick sheet of plastic is placed on the top and bottom

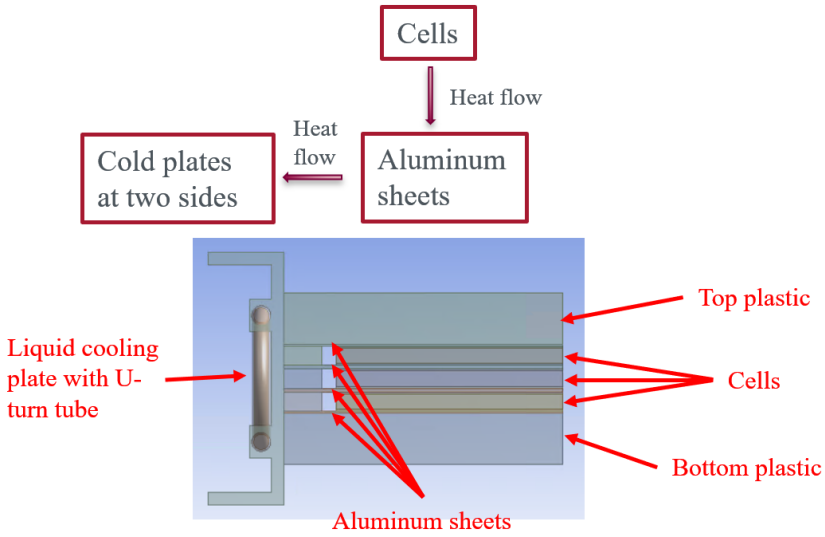

Figure 4.2: Schematic of the heat flow in half edge cooling CAD

surfaces of the cell stack to prevent heat flow out of these surfaces and provide structural rigidity. The module design effectively emulates a symmetric three-cell stack sliced out of a long stack of cells in a full-size vehicle battery pack. Thermal pads, as mentioned above, are used between the aluminum sheets and the cells to achieve the desired surface contact and enhanced heat transfer. At the two sides of the modules, aluminum bars are used to fill the gaps between the aluminum sheets and enhance the thermal contact between the aluminum sheets and the cold plates. The liquid cold plates on the two sides are manufactured by Wakefield-Vette, part number 180-11-12C, and utilize a 3/8 inch rolled copper tube attached to the aluminum base. These cold plates are bolted to the machined flat surface of the edge of the module, with thermal grease placed in between, ensuring a very thermally conductive connection.

4.2.3 Inter-Cell Cooling Module Design

For inter-cell cooling, liquid cooling plates which are just a couple of millimeters thick would typically be used so that the volume of the pack is not too large. It is very difficult to manufacture such thin cooling plates though; a process of stamping the cooling channel and bonding thin metal plates together would be needed. As a compromise, thicker more easily manufacturable liquid cooling plates, as shown in Figure 4.3, were designed and built.

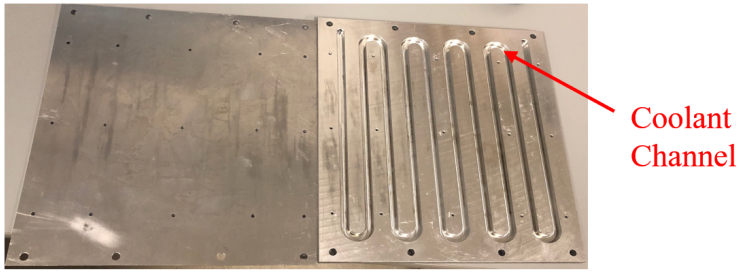

Figure 4.3: Disassembling view of the inter-cell cooling plate

The cooling plates consist of a bottom 9.5mm thick aluminum sheet with a serpentine cooling channel machined into it. The coolant flows in and out of threaded holes at either end of the cooling channel. When assembling, a silicone gasket sealant for use in mechanical assemblies, part number 038-3816-4, is applied on the mating surfaces surrounding the coolant channel, and the 2mm thick top plate is screwed on via several flush mount screws distributed across the surface. The configuration of the inter-cell cooling module is similar to the edge cooling module. Identical cells, thermal pads, aluminum bars, and plastic sheets are used, but the four interlaid aluminum sheets are swapped with the newly designed inter-cell cooling plates. The fully assembled module is presented in Figure 4.4, with the schematic of the heat flow and the half CAD drawing in Figure 4.5.

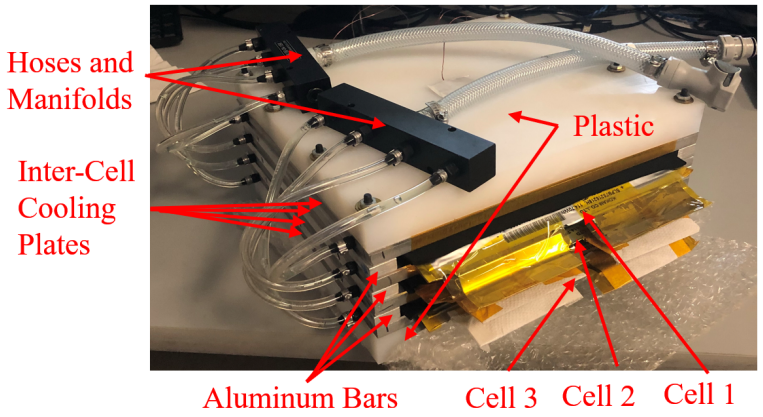

Figure 4.4: Configuration of the inter-cell cooling module

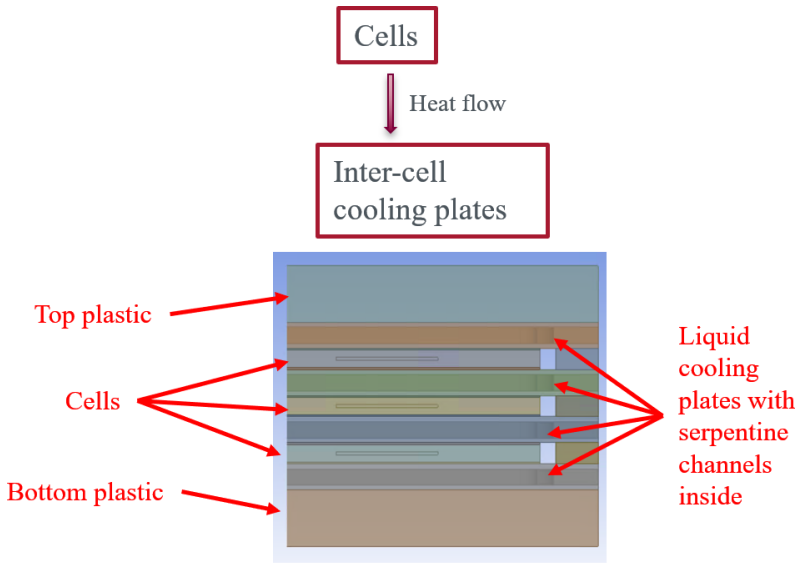

Figure 4.5: Schematic of the heat flow in half inter-cell cooling CAD

4.2.4 Test Equipment, Data Logging, and Instrumentation

To regulate the temperature of the battery module, the cell modules are tested in a Thermotron SE-3000-6-6 environmental chamber. All the tests are conducted with an ambient and coolant temperature of 20℃ to emulate typical conditions. The

cell is charged and discharged with a Digatron Power Electronics MCT 75-0/5-8ME cell cycler. Temperature data logging is achieved by LabVIEW using a National Instruments NI-9213 data acquisition module. A 6L, 200W, VWR 1160S refrigerated heated circulating bath chiller is used to circulate the coolant for the cold plates of the edge cooling module. The inter-cell cooling module uses a 1200W LS51MX1A113C centrifugal pump chiller from PolyScience. Both chillers use a coolant of 50/50 glycol-water solution. Even though the two modules use different cooling systems, the associated heat loss from both modules during the tests is observed to be less than the rated power of the chillers, so the chillers are both able to maintain a constant coolant temperature.

Figure 4.6: Thermotron SE-3000-6-6 environmental chamber, in which the experiment apparatuses are placed

Figure 4.7: Digatron MCT cell cycler, 8 channels 75A current each, connecting the battery module with channel cables

To capture the detailed thermal behavior of the battery modules, fifteen type T thermocouples are placed in locations of interest throughout the module. Figure 4.8 shows five of the thermocouples on the middle cell of the edge cooling module. For the remaining ten thermocouples, two are placed at the center of the top and bottom cells like TC1 in Figure 4.8, two are at the middle cell edge close to the negative and positive tabs, one is at the center of the top aluminum sheet, two are at the inlet and outlet of the coolant, two are on the surfaces of the side cold plates (for the edge cooling module), and the last one is placed nearby the module to measure the ambient temperature. To provide a consistent comparison of the experimental results, the temperature profile at the middle of the center cell, TC1, is plotted for all test cases in this chapter.

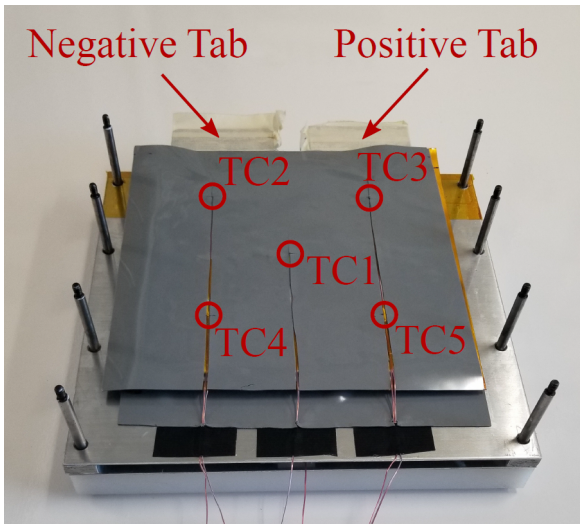

Figure 4.8: Thermocouple positions on the middle cell of edge cooling module

The edge cooling module has two inlets and outlets on the side opposite the battery tabs, the flow from or into the chiller is split into two hoses by a Y-shape connector, and enters or leaves the module. However, the inter-cell cooling module has four

cooling plates thus four inlets and four outlets. Four small-diameter hoses from the inlets or outlets merge the flow into one thicker hose by a manifold. The inlets of the cooling plates are at the side close to the battery negative tabs. As for the battery terminal connection, the edge cooling module has small intervals between the tabs, the upper and lower tabs are folded with a certain angle and are clamped with the middle tab by two aluminum bars that are connected to the power cable, Whereas the intervals between the tabs of the inter-cell cooling module are rather large, some machined aluminum cuboids are inserted between the tabs to provide good contact. It is noticeable that the power cables should be placed away from the temperature measurement unit to avoid the magnetic disturbance on the measurements. The final experimental apparatus layout for the edge cooling method is shown in Figure 4.9 and the inter-cell cooling method is shown in Figure 4.10.

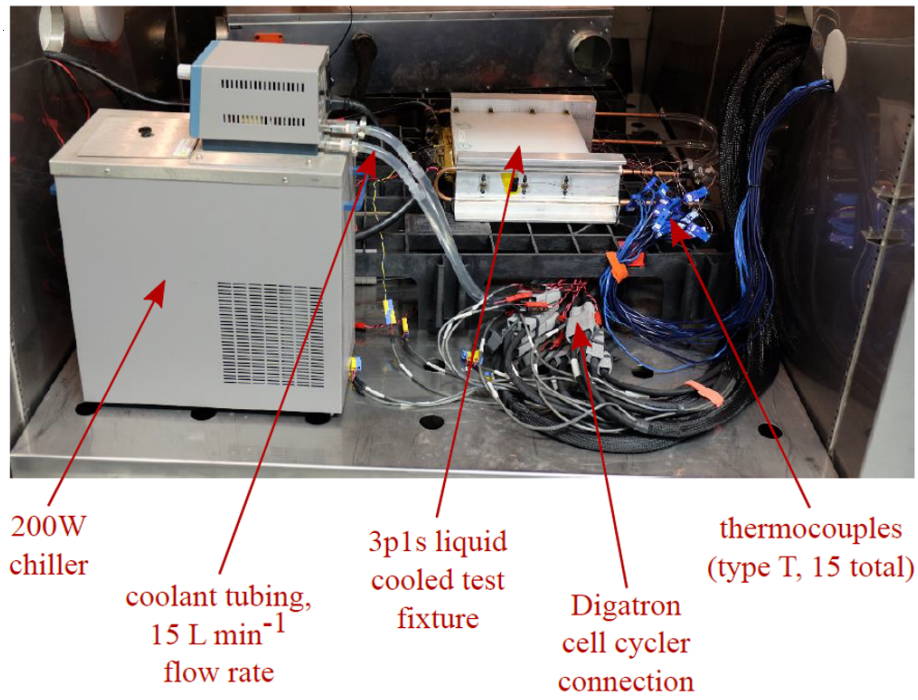

Figure 4.9: Edge cooling method experiment setup

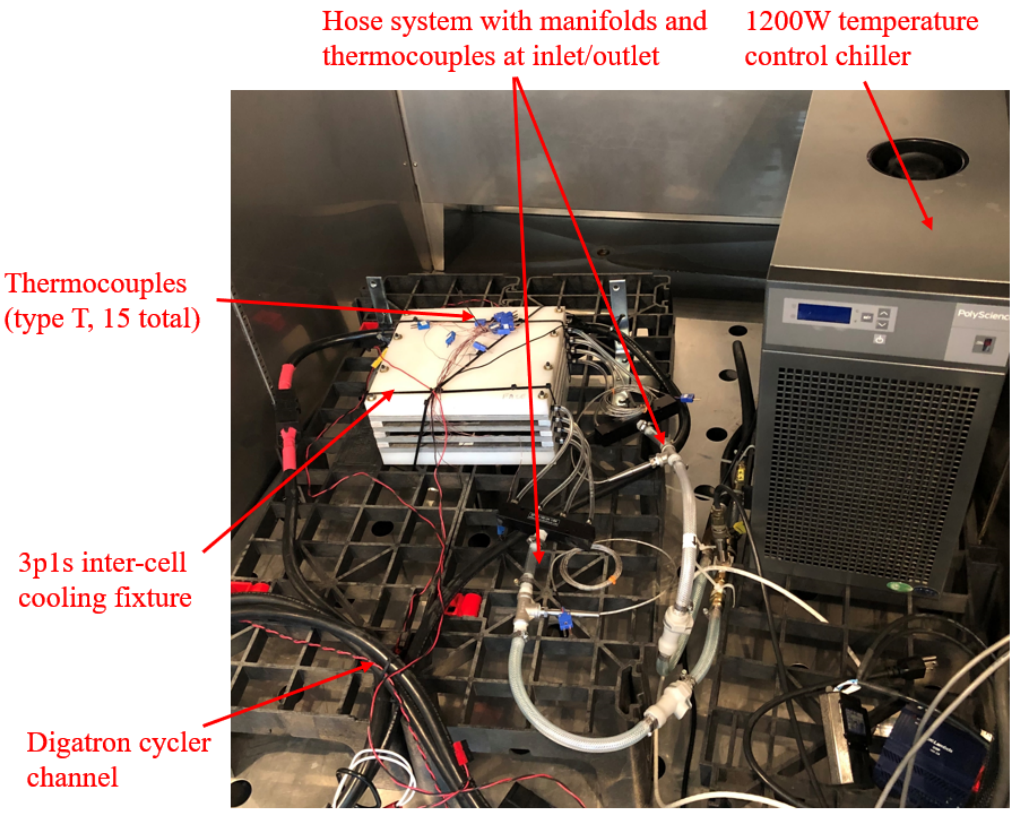

Figure 4.10: Inter-cell cooling method experiment setup

4.3 Description of Electrical and Thermal Characterization Tests

To provide insight into the performance of each module, three types of tests are designed and conducted on the modules. In the first test type, the thermal resistance of the module is determined from the temperature rise in response to various levels of heat generation in the cells. For the other two tests, the module's temperature response is measured for charging at rates of up to 5C and for an emulated road

trip where with repeated drive cycles and fast charges. Identical tests are performed on the two modules to provide an intuitive comparison of the active liquid cooling methods' behavior.

4.3.1 Thermal Resistance Test

The battery module thermal resistance describes how much the battery temperature will rise per unit of battery loss and is a key indicator of how effective a battery cooling system is. The thermal resistance is determined by creating a steady-state loss in the battery module and measuring the temperature rise for that loss. The cycler is used to apply a zero average current square wave to the module as shown in Figure 4.11, such there is no net charge supplied to the cell. All of the energy input to the cell is therefore loss, and the loss power can be calculated as measured energy divided by time as in Figure 4.12, the slope of the accumulated cycler energy profile is the constant power loss from the battery module. For the test program, the cycler first discharges the battery module to around 70% SOC to avoid hitting the upper or lower voltage limits during the test. Then the module is discharged at a constant current for 6 seconds and charged for approximately 6 seconds until the discharged amp-hours have been returned to the cell. The charge and discharge pulses are repeated for about 1.5 hours, long enough for the temperature to be steady-state for a period of time.

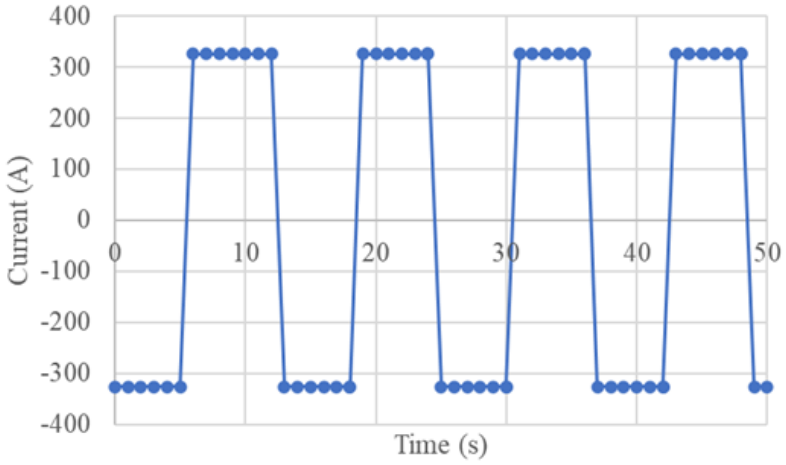

Figure 4.11: 50 seconds of the cycler current for 3.5C thermal resistance test

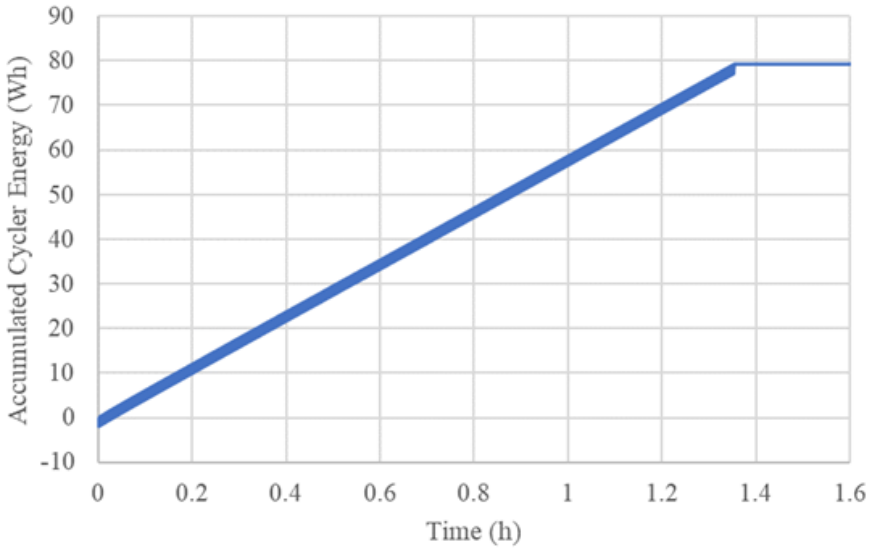

Figure 4.12: Measured accumulated cycler energy for 3.5C thermal resistant test of the inter-cell cooling module, the slope is 57.83W for the battery module, each cell has 19.28W power loss.

The test is repeated for currents of 1.5C, 2C, 2.5C, 3C, and 3.5C. The energy output from the cycler is recorded so that the power loss from the cells can be calculated. With the power loss, P_{loss}, and measured temperature rise, ΔT, the thermal

resistance, R_{therm}, at a selected position in the module can be calculated by:

$$R_{therm} = \frac{\Delta T}{P_{loss}} \tag{4.1}$$

4.3.2 Ultra-Fast Charging Test

The most challenging case for an EV battery module is ultrafast charging, where there is a very high loss for a short, transient period of time. The temperature during the fast charge is a function of both the thermal resistance, as measured in the last subsection, as well as the thermal heat capacity of the module which will absorb some portion of the loss. Elevated temperature is a key factor that results in degradation and damage to the battery, and temperature rise under fast charging is, therefore, an important indicator of the TMS performance. For the fast charging tests, the battery is first discharged to around 0% SOC at a 0.5C constant current and is then charged with constant current at 1C, 2C, 3C, 4C, and 5C rates. The constant current is continued until a voltage of 4.2V is reached, and voltage is then regulated until the current falls below 0.1A. Each charge test is repeated twice for consistency. The cycler current to the battery module for a 5C ultra-fast charging test is shown in Figure 4.13.

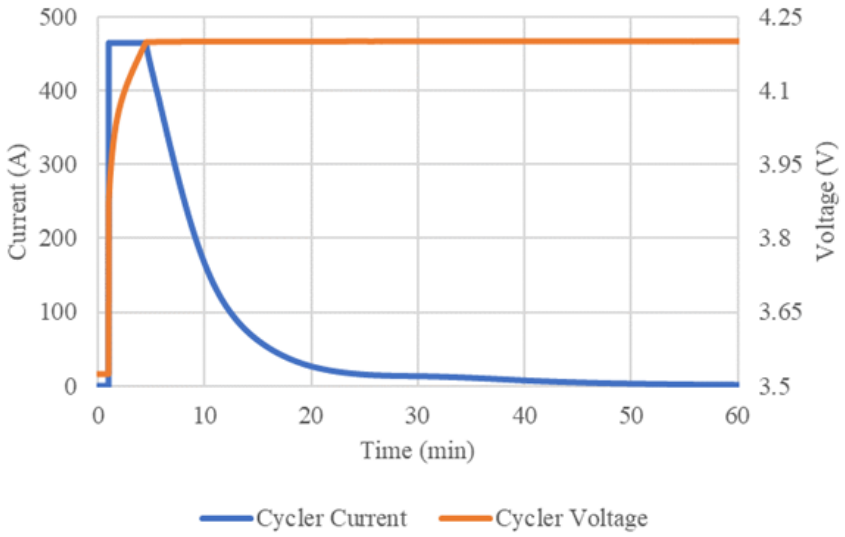

Figure 4.13: Cycler current and voltage for 5C ultra-fast charging test

4.3.3 Road Trip Test

To demonstrate how battery temperature varies during typical vehicle operations, the battery modules are tested with a series of drive cycles and fast charges. A US06 drive cycle power profile is calculated with a model of a 2018 Nissan Leaf with a 40kWh battery pack. The power is scaled for the tested battery module and the US06 cycles are repeated until the battery is empty. The module is then charged at a constant current of 4C magnitude to 4.2V and constant voltage at 4.2V until the current falls to 1C, resulting in a charge of around 85% to 90% SOC. The process is repeated several times to demonstrate how well the battery temperature is maintained over a long series of drives and fast charges. Figure 4.14 shows the cycler current for the road trip test, and Figure 4.15 shows the battery SOC.

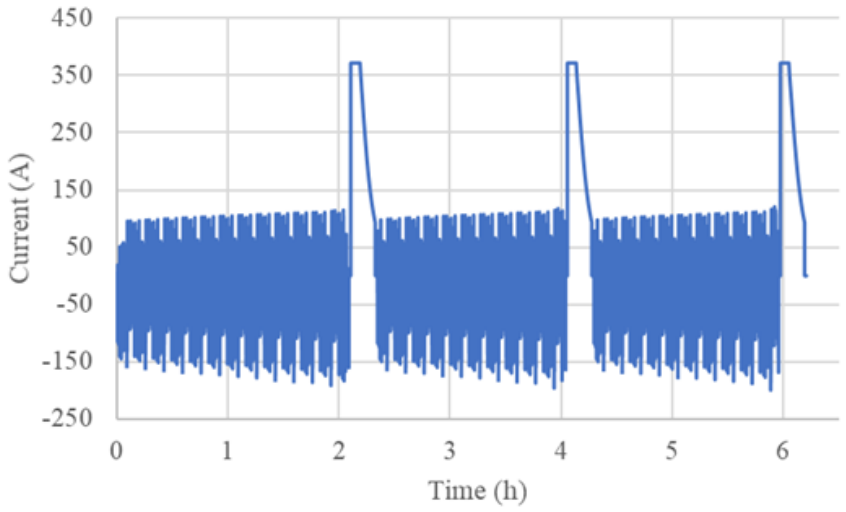

Figure 4.14: Cycler current for road trip test

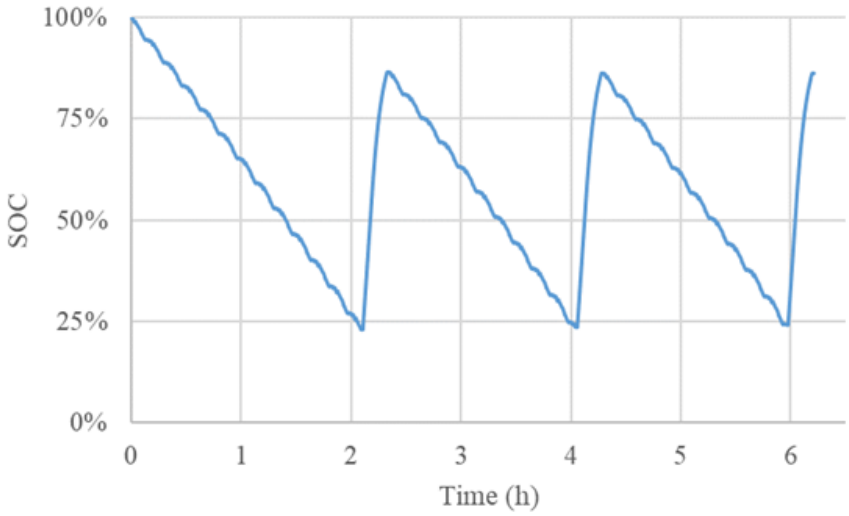

Figure 4.15: Battery SOC for road trip test

4.4 Experimental Results and Discussion

The measured temperature rise for square wave current magnitudes varying from 1.5C to 3.5C in 0.5C increments is plotted in Figure 4.16. The loss per cell ranges from 4 to 16W for the edge cooling module and is somewhat higher, from 4 to 19W, for the intercell module because the batteries aged somewhat prior to performing the inter-cell tests. The steady-state temperature rise versus the measured loss is plotted in Figure 4.16c, showing that the edge cooling module has a thermal resistance of 0.52°C/W and the intercell module resistance is just 0.08°C/W, a more than 80% reduction.

For the ultra-fast charging test, the measured temperature versus time for five current magnitudes is shown in Figure 4.17. An increasing charging rate results in a higher temperature rise. A peak temperature of 34.2°C for the 5C charge rate test is observed for the edge cooling module and 24.1°C for the inter-cell module. The inter-cell module is clearly able to remove heat from the module much more effectively, which is important because battery temperature is typically limited to 40 or 45°C during charging. The inter-cell cooling module could utilize a much higher coolant temperature without exceeding the charging temperature limit, potentially allowing for faster charging when temperatures outside the vehicle are high.

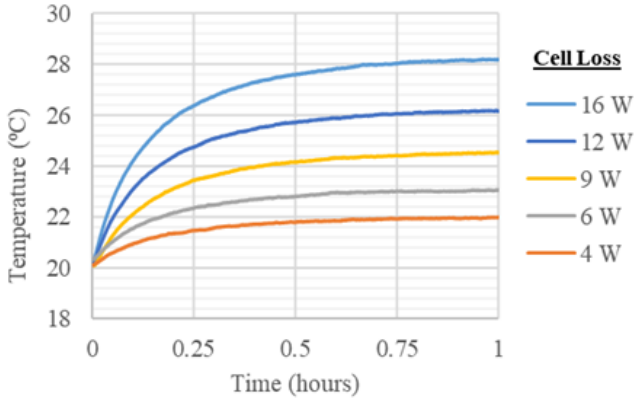

(a) Edge cooling module, temperatures vs. cell loss

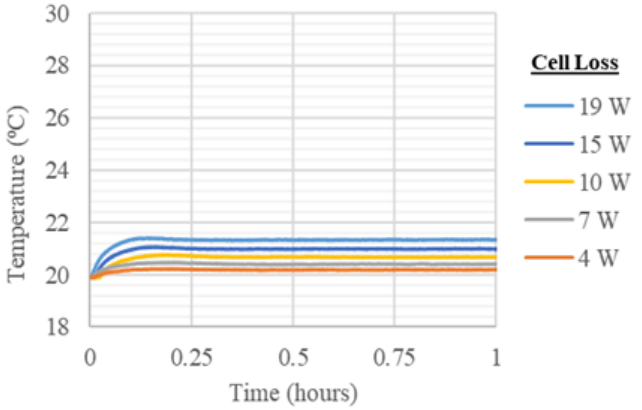

(b) Inter-cell cooling module, temperatures vs. cell loss

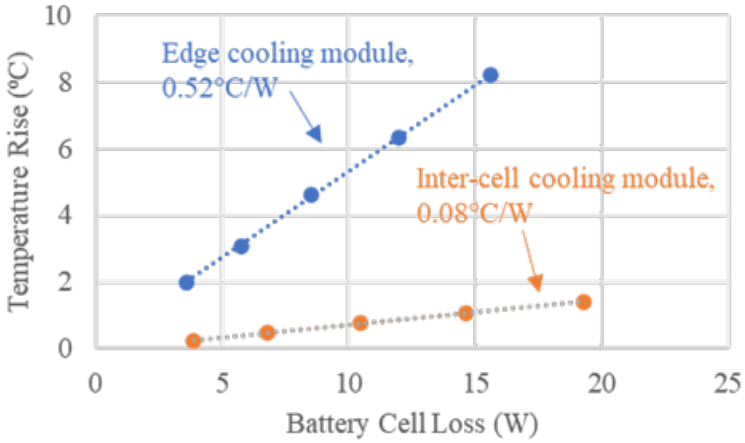

(c) Thermal resistance comparison

Figure 4.16: Thermal resistance test temperature response

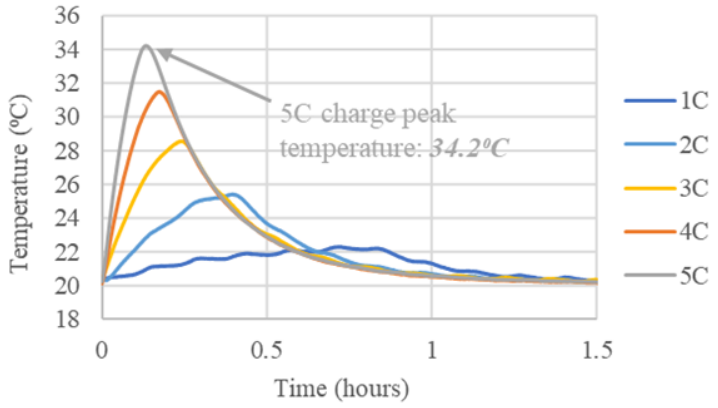

(a) Edge cooling module, fast charging temperature

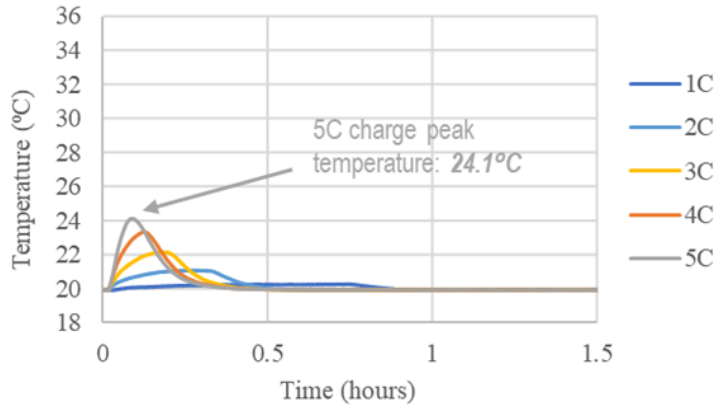

(b) Inter-cell cooling module, fast charging temperature

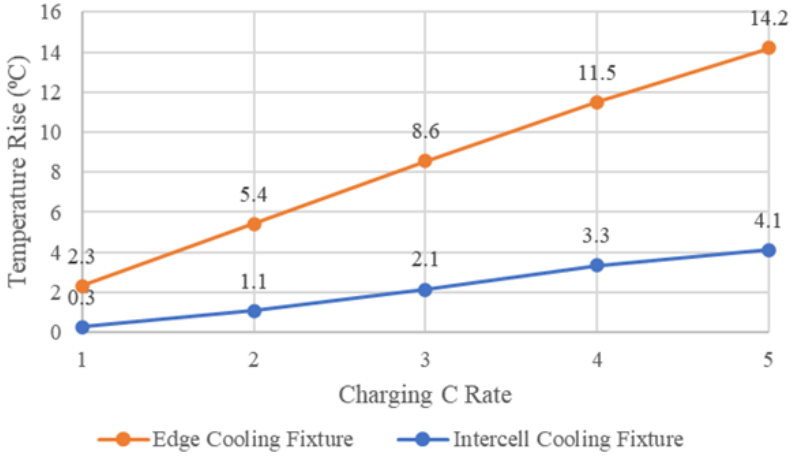

(c) Fast charging temperature rise of two modules

Figure 4.17: Ultra-fast charging test temperature response

The inter-cell cooling module also has a faster thermal time constant; for a 5C rate charge, for example, the temperature drops from the peak temperature to 21°C in 8 minutes while the edge cooling module takes 40 minutes. Temperature rise versus charge rate is plotted in Figure 4.17c, showing that temperature rise is significantly lower for the intercell module.

Figure 4.18 shows the temperature profiles for the inter-cell cooling module and edge cooling module during the road trip test. The drive cycle part does not generate much heat, so the temperature variation is not significant, while the ultra-fast charging part has an evident temperature rise. Similar to the ultra-fast charging test, the inter-cell cooling module has less temperature rise and temperature also reduces more quickly following the fast charge. One notable observation is that the length of the inter-cell cooling battery module test is about 20% shorter than the edge cooling battery module test. This is mostly a result of aging; the edge cooling tests were performed about a year prior to the edge cooling tests and the battery aged somewhat in that period contributing to a reduction in the SOC window for the intercell tests. Overall, it is important that the TMS provides fast thermal control as demonstrated. An insufficient system will result in heat accumulation, i.e., there will not be enough time for the temperature to drop down, and repeated driving and charging events will lead to an even higher temperature or a reduction in achievable charge rate.

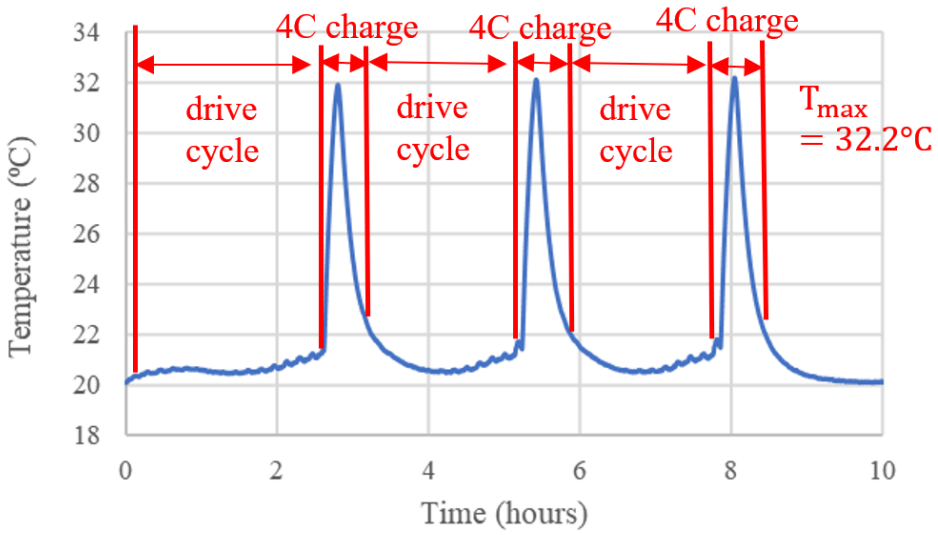

(a) Edge cooling module road trip temperature

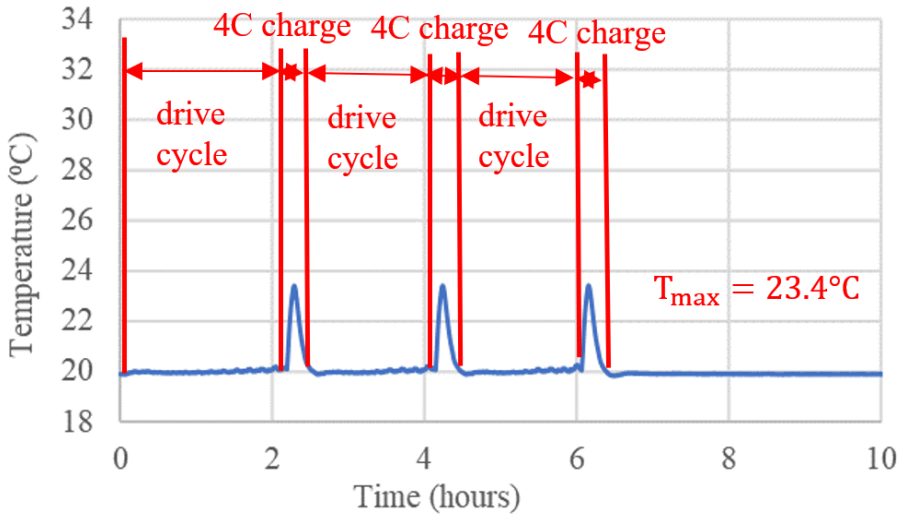

(b) Inter-cell cooling module road trip temperature

Figure 4.18: Road trip test temperature response

4.5 Summary

Two ultrafast charging battery modules with Kokam NMC 31 Ah pouch cells were developed. One module utilized a simpler cooling method, with coolant flowing along

the edges of the module (edge cooling), and the second had coolant flowing between the cells (inter-cell cooling).

Overall, the inter-cell cooling module was observed to have a much lower thermal resistance, thus having lower temperature rise and faster thermal response compared to the edge cooling module. For the highest charge rate of 5C the edge cooling module had 14.2°C temperature rise, while the inter-cell module had just 4.1°C rise, demonstrating that the inter-cell module could utilize a higher coolant temperature or charge at even faster rates. Likewise, during repeated drive cycles and fast charges, the inter-cell module had a temperature rise of just 3.4°C while the edge cooling module had a 12.2°C rise. However, the inter-cell cooling module has a complex configuration that the adds expense of fabricating, assembling, and sealing a multitude of thin cooling plates, making it more expensive to manufacture than edge cooling. When evaluating a cooling technology for an application, it is important to consider multiple module cooling system designs, as is done here, in conjunction with the fast charging requirement, the loss generated by the cells, the aging impact of temperature, and method of removing heat from the coolant.

Chapter 5

Heat Generation and Thermal Modeling of the Inter-Cell Cooling Battery Module

5.1 Introduction

In this chapter, a heat generation model is developed for the Kokam NMC cells by considering both reversible and irreversible loss. The reversible loss is a function of the battery current, temperature, and the entropic heating coefficient as a map obtained from the experiment. The irreversible loss is a sum of the joule heating of the battery and the dissipated energy in electrode polarization. The total loss, as the heat input to the thermal models, is assumed to be distributed uniformly by volume on the pouch cells.

The CAE-based thermal models including a CFD-based steady state model and a thermal-only transient state model are built in ANSYS as a numerical simulation of

the inter-cell liquid cooling battery module that was designed and tested in Chapter 4. The steady state model is built in ANSYS Fluent to capture more fluid dynamics of the coolant flow, the heat transfer coefficient between the coolant flow and the coolant channels inside the inter-cell cooling plates is calculated after performing the steady-state simulation. Afterward, the calculated heat transfer coefficient is applied in the transient state model, the transient numerical simulation can be much simpler and faster to conduct due to saving from the calculation of the coolant flow dynamics. With the time-varying heat generation rate from the loss model, the thermal-only transient state model can simulate the temperature behavior of the battery module under the desired test.

5.2 Heat Generation and Battery Loss Model

In order to capture the thermal characteristics of a battery, a reliable heat generation model is required as the loss input to the thermal model to result in the temperature change. Bernardi et al. in (Bernardi *et al.*, 1985) started from the general energy balance for a battery system, the battery temperature was assumed to be uniform throughout the cell, its change with time was determined by the chemical reactions, changes in the heat capacity of the system, phase changes, mixing, electrical work, and heat transfer with the surroundings. The equation of the cell loss was developed and derived in a complete and general manner. In a simplified form, the total internal heat generation rate of the battery was the sum of the irreversible loss and reversible loss. It was given by the energy balance equation as:

$$\dot{Q}_{total} = \dot{Q}_{irrev} + \dot{Q}_{rev} = I(OCV - V_T) - IT\frac{\partial OCV}{\partial T} \tag{5.1}$$

where I is the current in Ampere (positive for discharge), T is the uniform battery temperature in Kelvin, OCV is the open-circuit voltage in Volt, V_T is the terminal voltage in Volt. For the irreversible loss term, the difference between OCV and terminal voltage gives the cell overpotential, which indicates the irreversibilities such as ohmic losses, charge-transfer polarization, and mass-transfer limitations. The irreversible loss consists of the joule heating of the battery and the dissipated energy in electrode polarization. The reversible loss is the result of reversible isothermal cell operation which is the entropic change.

When calculating the total internal heat generation rate of the battery, most of the terms in the equation can be directly measured or obtained from a general characterization test like that the OCV data is provided by the HPPC test. However, the entropic heating coefficient term as $\partial OCV/\partial T$ in reversible loss cannot be easily got. As a matter of fact, many researchers neglect the reversible loss due to a lack of data on the entropic heating coefficient, and the amount of the reversible loss is insignificant when compared with the irreversible loss under high discharge rates(Srinivasan and Wang, 2002). As further grounds for neglecting the term in HEV application, the net reversible heat effect of a battery pack is close to zero over typical drive cycle (Smith and Wang, 2006a).

To provide an accurate heat generation rate and thus a high-fidelity thermal model, the loss model including both reversible and irreversible loss calculation will be considered in this work. Lempert et al. in (Lempert *et al.*, 2020) performed an elaborated experiment to measure the battery entropic heating coefficient as a function of battery SOC and temperature, the effect of battery self-discharge and voltage relaxation was corrected by extracting the rate of change of OCV at steady state

and formed a lookup table. As a reference of the cell with identical chemistry, the reversible battery loss in this work is established following the measured entropic heating coefficient map.

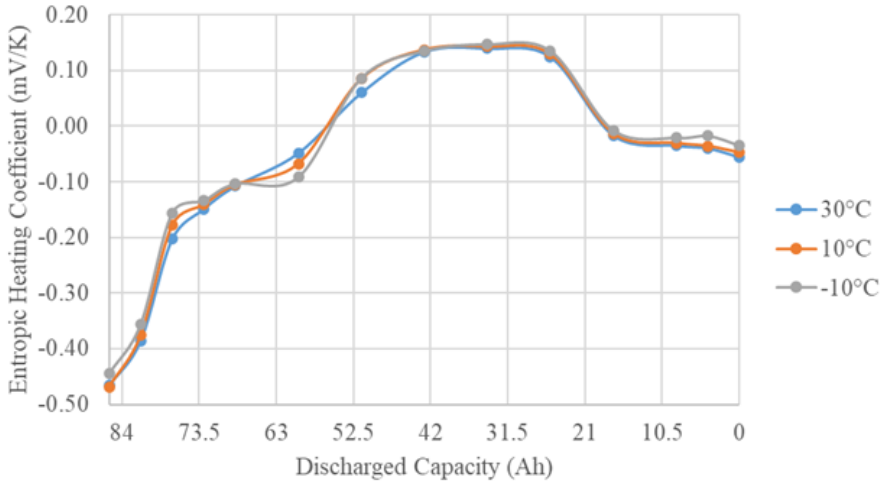

Figure 5.1: Entropic heating coefficient map

A set of characterization tests including the HPPC test, capacity test were carried out to calibrate the inner resistance, OCV, and available capacity. As the battery module was aged prior to performing the inter-cell cooling experiment, the battery capacity was faded somewhat when compared with the rated value. From the entropic heating coefficient map, the maximum discharged capacity is 85.72Ah, while the rated capacity is 91Ah for the battery module. Furthermore, the entropic heating coefficient varies little with the test temperatures. A relatively large negative coefficient value at large discharged capacity or low SOC is observed, which indicates that there is a large amount of entropic heat absorbed by the batteries when charging or a large amount of entropic heat dissipated when discharging at the depleted state of the battery.

With the entropic heating coefficient, other parameters can be obtained from

measurement or characterization test, the battery module loss can be modeled by Equation 5.1. Particularly, the terminal voltage can be calculated by some modeling techniques such as the equivalent circuit model. In this way with a characterized battery, the terminal voltage can be modeled without any experimental testing. In this work, the battery module losses of 1C, 3C, 5C ultra-fast charging and the road trip tests are modeled, the input data including current, temperature, terminal voltage to the loss model are from the experimental measurement in Chapter 4. It can be seen that the percentage of the reversible loss to the total loss decreases as the charge rate increases, it is around 24% of the total loss for 1C charging and around 8% for 5C charging. This can be explained by the loss model equation, the irreversible loss growing one order of magnitude more than the reversible loss as the current increases. In addition, the contribution of the reversible loss decreases as the temperature decreases.

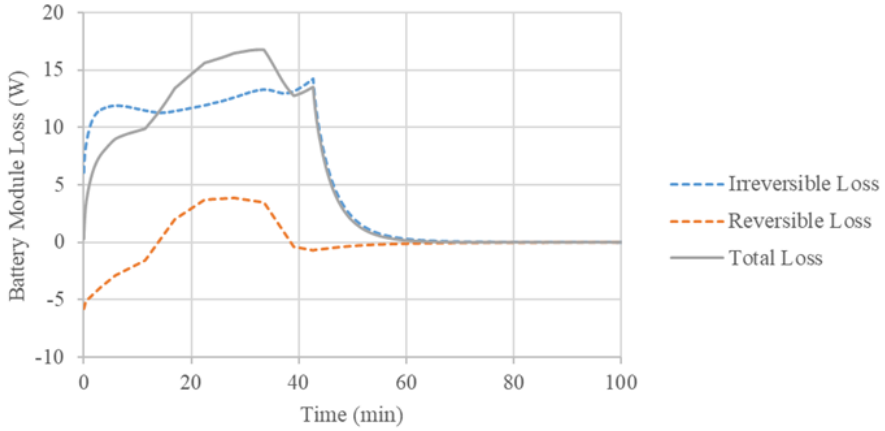

Figure 5.2: Modeled battery module loss for 1C ultra-fast charging, the peak reversible loss is around 24% of the peak total loss

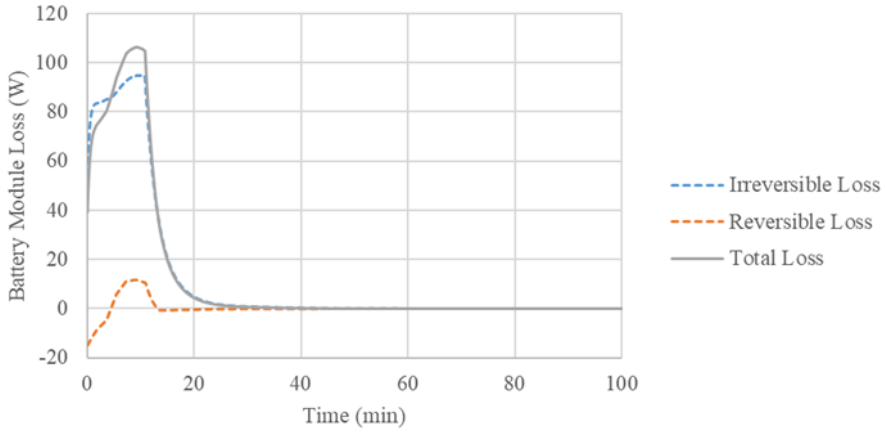

Figure 5.3: Modeled battery module loss for 3C ultra-fast charging, the peak reversible loss is around 10% of the peak total loss

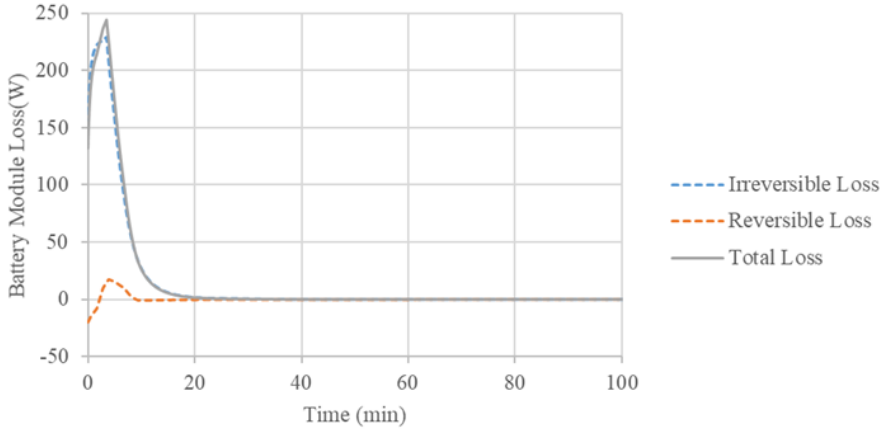

Figure 5.4: Modeled battery module loss for 5C ultra-fast charging, the peak reversible loss is around 8% of the peak total loss

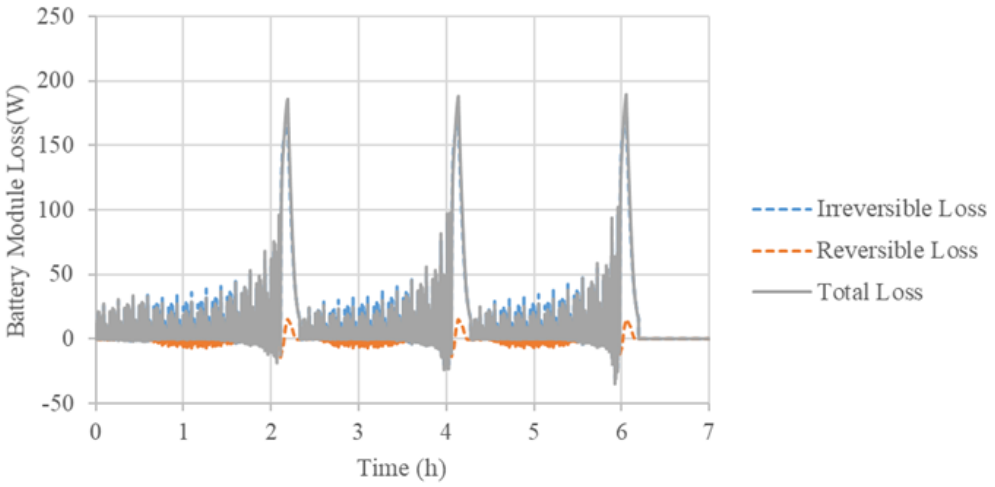

Figure 5.5: Modeled battery module loss for a road trip with repeated US06 drive cycles and 4C ultra-fast charging, the drive cycle part generates less heat, the peak loss of 4C ultra-fast charging is between the peak loss of 3C and 5C ultra-fast charging

5.3 Development of the Inter-Cell Cooling Battery Module Thermal Model

5.3.1 CFD-Based Steady State Model

The steady state model is built in ANSYS Fluent, it simulates the fluid dynamics of the coolant flow, and calculates the heat transfer between the coolant and the battery module. In ANSYS Fluent, conservation equations for mass and momentum are solved by FEA. As the flow involves heat transfer, an additional equation for energy conservation is required (ANSYS, 2009). Equation 5.2 is the general form of the mass conservation or continuity equation, Equation 5.3 is the conservation of

momentum in an inertial reference frame, Equation 5.5 is the energy equation.

$$\frac{\partial \rho}{\partial t} + \nabla \cdot (\rho \vec{v}) = S_m \tag{5.2}$$

where ρ is the fluid density, $\vec{v}$ is the velocity vector field of the fluid. S_m is the mass added to the continuous phase from the dispersed second phase such as the vaporization of liquid droplets, it can also be any user-defined sources.

$$\frac{\partial}{\partial t}(\rho \vec{v}) + \nabla \cdot (\rho \vec{v} \vec{v}) = -\nabla p + \nabla \cdot (\overline{\overline{\tau}}) + \rho \vec{g} + \vec{F} \tag{5.3}$$

where p is the static pressure, $\rho \vec{g}$ and $\vec{F}$ are the gravitational body force and external body forces. $\vec{F}$ can also be model-dependent source terms such as porous-media and user-defined sources. $\overline{\overline{\tau}}$ is the stress tensor, given by:

$$\overline{\overline{\tau}} = \mu[(\nabla \vec{v} + \nabla \vec{v}^T) - \frac{2}{3} \nabla \cdot \vec{v} I] \tag{5.4}$$

where μ is the molecular viscosity, I is the unit tensor, the second term on the right side of the equation is the effect of volume dilation.

$$\frac{\partial}{\partial t}(pE) + \nabla \cdot (\vec{v}(\rho E + p)) = \nabla \cdot (k_{eff} \nabla T - \sum_j h_j \vec{J}_j + (\overline{\overline{\tau}}_{eff} \cdot \vec{v})) + S_h \tag{5.5}$$

$$E = h - \frac{p}{\rho} + \frac{v^2}{2} \tag{5.6}$$

where k_{eff} is the effective conductivity, which is k for laminar thermal conductivity and $k + k_t$ for turbulent thermal conductivity, k_t is defined by the turbulence model.

$\vec{J_j}$ is the diffusion flux of species j. The first three terms on the right side represent energy transfer by conduction, species diffusion, and viscous dissipation. S_h indicates the heat of chemical reaction, and any other user-defined volumetric heat sources. h is the sensible enthalpy.

By performing the steady state model calculation, the heat transfer coefficient between the coolants and the channels inside the cooling plates is given by:

$$h_{coolant} = \frac{q}{T_{surf} - T_{bulk}} \tag{5.7}$$

where q is the heat flux defined by the transferred heat per unit area of the coolant channel, T_{surf} is the area-weighted average surface temperature of the coolant and channel interface, T_{bulk} is the mass-average temperature of the coolant. These parameters can be obtained after the thermal model calculation.

Geometry, Component Properties and Model Reduction

The geometry of the steady state model is designed based on the inter-cell cooling battery module in the experiment in Chapter 4, some details are ignored without making much difference on the simulation accuracy such as the fixation of the flush mount screws on the cooling plates, bolts, and holes on the components throughout the battery module, battery tabs. The cross-section of the coolant channels on the cooling plates is 0.29in×0.3in. The thermal properties of the cell are scaled by the density ratio of a battery with the similar chemistry and manufacturer that was measured in (Nieto *et al.*, 2014), the in-plane (xy-plane as shown in Figure 5.7) conductivity for the cell is 22.2W/m·K, and 1.03W/m·K through-plane. The dimensions and material properties of the rest components are given in Table 5.1. In FEA simulation, a symmetric boundary condition is used when the physical geometry and the

thermal solution have mirror symmetry to reduce the computational effort greatly. In this steady state model, the coolant flow is perpendicular to the height of the battery module, therefore no symmetric plane that is perpendicular to the length/width surface can be placed. Although the coolant channel is not situated right at the center of the cooling plate thickness direction, the deviation is just around 0.05mm, it is suitable to place the symmetric plane at the height center and perform simulation on half of the battery module.

Table 5.1: Dimensions and properties of the inter-cell cooling battery module components

Component	Material	Dimension $L \times W \times H$	Density (kg/m^3)	Specific Heat Capacity (J/kg·K)	Thermal Conductivity (W/m·K)
Cooling Plate (top)	Aluminum 3003-H4	$11 \times 10 \times 0.081(in)$	2800	900	180
Cooling Plate (bottom)	Aluminum 3003-H4	$11 \times 10 \times 0.375(in)$	2800	900	180
Thermal Pad	Tflex HR440	$228.32 \times 227 \times 0.86(mm)$	-	-	1
Aluminum Bar	Aluminum 6061-T6511	$254 \times 19.05 \times 9.525(mm)$	2700	900	170
Plastic	UHMW Polyethylene	$11 \times 10 \times 1(in)$	940	1750	0.41
Kokam NMC Cell	-	$228.32 \times 227 \times 7.8(mm)$	1799	813	-

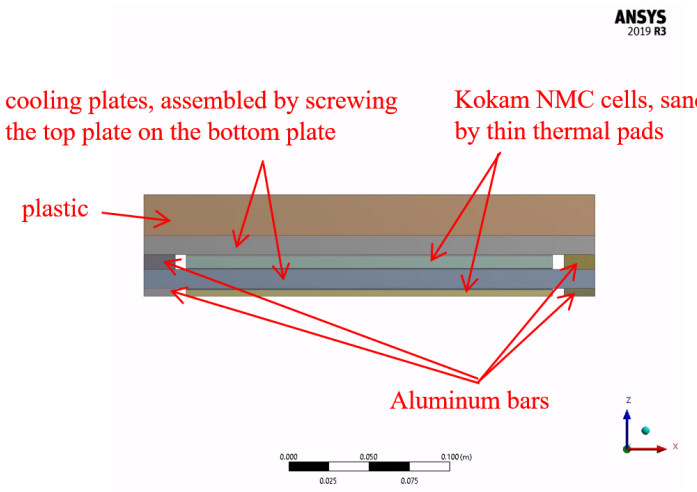

Figure 5.6: CAD of the half battery module on xz-plane, demonstration of components

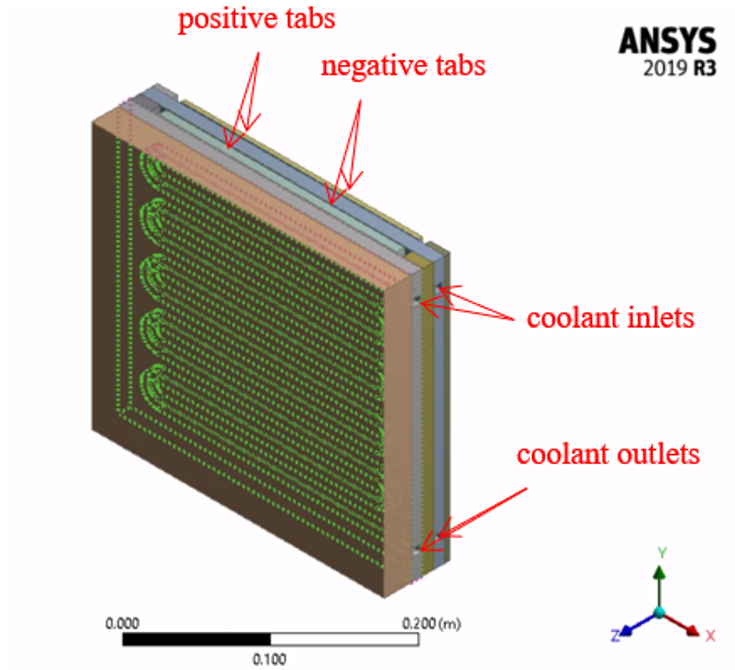

Figure 5.7: CAD of the half battery module on z-axis, the highlighted inner edges enclose the coolant flow channel in the top cooling plate, battery tabs are not considered in the thermal analysis

Selection of Viscous Model for the Coolant

ANSYS Fluent provides many viscous models to simulate inviscid, laminar, and turbulent flow. To determine the coolant flow pattern in this thermal model, the Reynolds number as the ratio of inertial forces to viscous forces needs to be calculated. The Reynolds number is defined as:

$$Re = \frac{\rho u d_h}{\mu} \tag{5.8}$$

where ρ is the coolant density, u is the velocity based on the actual cross section area of the coolant channel, μ is the coolant dynamics viscosity, d_h is the hydraulic diameter of the coolant channel, and is given by:

$$d_h = \frac{4A}{p} \tag{5.9}$$

where A is the cross section area and p is the perimeter of the coolant channel. The coolant used in the inter-cell cooling battery module is 50/50 propylene glycol-water solution, the properties are obtained from (CWG, 1991). The maximum flow rate that the chiller can provide in the inter-cell cooling experiment is 10L/min based on the specification, the corresponding Reynolds number is calculated as 927. As a matter of fact, the coolant flow pattern involved in this work is laminar.

Cell Zone and Boundary Conditions

Heat transfer coefficient is a function of the thermal properties of the medium, the hydrodynamic characteristics of the flow, and the hydrodynamic and boundary conditions (Kurganov, 2011). To carry out the calculation of the heat transfer coefficient of the coolant inside the channel, a source term is required to have the energy input

to the steady state thermal model. Previous experimental work indicates that the cell will generate 19W constant power loss during the 3.5C thermal resistance test, normalized by the cell volume, the energy source with $47006.43 W/m^3$ is assigned to the battery cell zone.

When building the geometry and mesh of the steady state model, all the parts of the battery module are named separately, some surfaces such as the coolant inlets and outlets, symmetry at the height center, all the surfaces that are exposed to the ambient environment, and interfaces between the parts are also grouped as named selections. ANSYS Fluent solver can read the named selections and categorize the boundary conditions accordingly. The coolant inlet velocity is 0.7423m/s to simulate 10L/min coolant flowing through the battery module, and the inlet temperature is assumed to be 20°C. The outlet boundary condition is pressure-outlet with 0Pa gauge pressure. All the interfaces between the parts are thermally coupled so the solids have heat conduction ignoring any contact loss. The coolant flow and the channels are also coupled, and the heat transfer between is mainly heat convection. The rest surfaces exposed to the ambient environment are set to be adiabatic walls, so the heat generated by the cells is purely removed by the coolant flow. A symmetry at the height center is set so that a mirror heat transfer is assumed in either half of the battery module.

Mesh Sensitivity Study

FEA software solves equations at cell/nodal locations, the domain is required to be divided into discrete cells that is called meshing. Even though the geometry of the battery module is regular and simple, a good mesh can improve the efficiency and accuracy of the calculation. The steady state model uses tetrahedral element

meshes mostly as well as a few hexahedral and wedge element meshes. The sweep method with quad/tri free face mesh type is applied on the cells and thermal pads, the source and target faces are the pouch surfaces of the cells and the contact surfaces between thermal pads and other parts. Coolants and cooling plates use the body sizing method, and the inflation method is utilized on the plastic sheet and aluminum bars. The overall mesh quality is determined by the user-defined element size. A mesh sensitivity study is conducted to compare the mesh quality based on the calculated heat transfer coefficient from Equation 5.7, the computation effort of each mesh is also recorded. The results are summarized and presented in Table 5.2.

Table 5.2: Mesh comparison by the heat transfer coefficient values, the numbers of mesh nodes and elements, and the computation time. The error is based on the coefficient value of the finest mesh

	Coarse Mesh	Middle Mesh	Fine Mesh	Extra Fine Mesh
Number of Mesh Nodes	904735	1752362	2443153	4850028
Number of Mesh Elements	3795940	7411651	10008479	15299700
Heat Transfer Coefficient ($W/(m^2K)$)	499.17	612.24	686.94	708.30
Error of Heat Transfer Coefficient	29.53%	13.56%	3.02%	baseline
Estimated Computation Time (min)	8	20	35	75

Although the finest mesh takes much computation time, the heat transfer coefficient only needs to be calculated for a single time, and CFD calculation demands a high-precision meshing to get an accurate result. Therefore, the finest mesh result of the steady-state model is considered, the calculated heat transfer coefficient of the coolant flow inside the channels is $708.30 W/(m^2K)$.

5.3.2 Thermal-Only Transient State Model

The thermal-only transient state model is built in the transient thermal analysis system in ANSYS. The objective of the transient state model is to solve the energy equation with some thermal quantities that vary over time. The governing equation for the transient state analysis is the first law of thermodynamics integrated with heat conduction on a differential control volume (ANSYS, 2020):

$$k(\frac{\partial^2 T}{\partial x^2} + \frac{\partial^2 T}{\partial y^2} + \frac{\partial^2 T}{\partial z^2}) + q = \rho c \frac{\partial T}{\partial t} \tag{5.10}$$

where k is the thermal conductivity, t is time, T is temperature, q is the rate of heat flux inside the volume, ρ is the density of the material, c is the specific heat of the material. The first term in the left side of the equation is the rate of heat conduction, the term in the right side of the equation is the rate of energy storage inside the volume.

In the transient state model, the geometry and component properties are replicated from the steady state model. However, the CFD of the coolant flow is dismissed, replaced with the convection heat term between the coolant channels and the ambient air. Since the numerical simulation of the coolant flow is no longer included, the transient model requires less accurate meshing to solve a simpler heat transfer phenomenon. From the previous experiment, the peak temperature rise of the coolant is less than 1°C, the temperature rise from inlet to outlet is less than 0.4°C. Therefore, the temperature of the ambient air nearby the coolant channels is assumed to be 20.1°C as the bulk mean temperature of the coolant flow.

Transient Thermal Analysis Settings

The initial temperature of the analysis is 20°C, it is also the controlled temperature

of the thermal chamber and chiller in the experiment. The internal heat generation is assigned to the cells, the magnitude is the input tabular data from the battery loss model. In the previous section, the loss model produced irreversible, reversible, and total loss of 1C, 3C, 5C ultra-fast charging and road trip tests. The transient state model applies the time-varying total loss per unit volume to the cells to simulate the battery heat generation behavior of the ultra-fast charging and road trip tests. A convection term is built to simulate the coolant convection to the coolant channels, ambient temperature is 20.1°C as the bulk mean temperature of the coolant flow, the film coefficient is the calculated heat transfer coefficient from the previous section as $708.30 W/(m^2K)$. The symmetry surface is defined as perfectly insulated so that a mirror heat transfer is assumed in either half of the battery module. In terms of the rest surfaces that contact with the surrounding air in the thermal chamber, another convection term with $20 W/(m^2K)$ film coefficient and 20°C ambient temperature to represent natural air convection between the battery module and the surroundings in the thermal chamber.

Mesh Sensitivity Study

Compared with the steady state model, the transient state model has a much coarser meshing since no coolant flow dynamics is simulated, and only heat convection and conduction are calculated on the rest parts as thermal masses. This model uses tetrahedral element meshes mainly, some hexahedral meshes and a few prism meshes. Sweep method with quad/tri free face mesh type is applied on the cells, the source and target faces are the pouch surfaces of the cells. The cooling plates use the body sizing method. The overall mesh quality is determined by the user-defined element size. A mesh sensitivity study is conducted to compare the mesh quality, 25 minutes

heat generation of a 5C ultra-fast charging test is performed on the transient state model, and the peak temperature rise from 20°C of each mesh is used as a benchmark. The computation effort of each mesh is also recorded. The results are summarized and presented in Table 5.3.

Table 5.3: Mesh comparison by the 5C charge peak temperature rise, the numbers of mesh nodes and elements, and the computation time. The error is based on the peak temperature rise of the coarsest mesh

	Coarse Mesh	Middle Mesh	Fine Mesh
Number of Mesh Nodes	33801	103607	301582
Number of Mesh Elements	14445	43505	139322
5C Charge Peak Temperature Rise (°C)	4.005	4.01	4.013
Error of Temperature Rise	baseline	0.1248%	0.1998%
Estimated Computation Time (min)	13	58	216

It is obvious that the quality of a mesh has little influence on the simulation accuracy, the finest mesh only improves around 0.2% from the coarsest mesh, while the execution time is 16 times longer. The transient state model needs to run for several tests, it is more important to budget the computation time. Therefore, the coarse mesh is used to validate the transient state model for the designed tests.

5.4 Summary

To build the thermal modeling of the battery module, the heat generation of the cells was first calculated. Both reversible and irreversible losses were considered using the simplified Bernardi heat generation model, where the entropic heating coefficient map cited from a similar work was utilized for the reversible loss calculation. After obtained the cell losses under 1C, 3C, 5C ultra-fast charging tests and a road

trip test, the CAE-based thermal models including a steady state model and a transient state model were established. The CFD-based steady state model in ANSYS Fluent simulated the dynamics of the coolant flow to calculate the heat transfer coefficient between the coolants and the coolant channels in the cooling plates. Then the thermal-only transient state model in ANSYS was constructed with the heat transfer coefficient from the steady state model and the heat generation rate from the loss model. Finally, a mesh sensitivity study was conducted on the steady state model and the transient state model, the meshing that gave a fine simulation result and took proper computation time was adopted for the simulation validation.

Chapter 6

Validation of the Inter-Cell Cooling Thermal Model and Comparison with the Experiment

6.1 Introduction

This chapter validates the inter-cell cooling thermal model built in the previous chapter, and the results are compared with the experimental measurements in Chapter 4. The thermal resistance test is validated on both the steady state model and transient state model to diagnose the thermal model quality. The ultra-fast charging tests including 1C, 3C, 5C-rate charging apply the heat generation rate from the loss model to the transient state model as energy input, and the calculated heat transfer coefficient from the steady state model is used by the transient state model to simulate the heat dissipation by the coolant. Finally, the temperature profile of the cell from the transient state model is obtained. Similar to the ultra-fast charging test, the road

trip test uses the heat generation rate of the loss model simulating a road trip with repeated US06 drive cycles and 4C ultra-fast charging to observe the cell temperature behavior. Moreover, a comparative study is conducted between the thermal modeling results and the experimental measurements to investigate the thermal modeling accuracy.

6.2 Validation of the Inter-Cell Cooling Thermal Model

6.2.1 Thermal Resistance Test Simulation

In the thermal resistance test, a constant power loss is assigned to the cells in both steady state model and transient state model, the FEA thermal models would reach a steady temperature state in the end. The heat generation rate from the loss model is replaced by the experimentally measured cell loss in Chapter 4, to avoid the errors by the loss modeling. Tests of 1.5C, 2C, 2.5C, 3C, 3.5C-rate with 4W, 7W, 10W,15W, 19W loss magnitude are performed, the maximum cell temperature rises from the initial temperature to the steady temperature state are recorded. It is observed that the temperature rise is a linear function of the battery cell loss, the slope is the thermal resistance which indicates the efficiency of the battery module cooling system.

Table 6.1: Thermal resistance test with measured cell loss and simulated temperature rises of both steady state model and transient state model

Measured Power Loss	Ambient/Initial Temperature (°C)	Peak Temperature Rise of the Cell (°C)	
		Steady State Model	Transient State Model
1.5C Test - 4W per cell	20	0.21	0.27
2C Test - 7W per cell		0.37	0.39
2.5C Test - 10W per cell		0.53	0.52
3C Test - 15W per cell		0.79	0.73
3.5C Test - 19W per cell		1.00	0.90

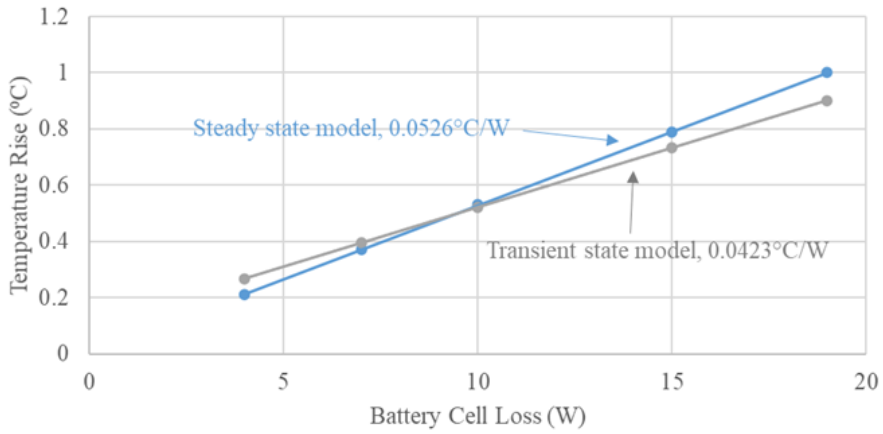

Figure 6.1: Simulated temperature rises are linear to the battery cell losses. The thermal resistance of steady state model is 0.0526°C/W, and transient state model is 0.0423°C/W

6.2.2 Ultra-Fast Charging Test Simulation

The ultra-fast charging tests are simulated by applying the heat transfer coefficient calculated from the steady state model to the contact surface of coolant and channel of transient state model, and the energy source on the cells is the heat generation rate obtained from the cell loss model. 1C, 3C, 5C-rate ultra-fast charging losses including

both irreversible and reversible losses were calculated in Chapter 5, the amounts of total losses are assigned to the cells as power per unit volume. The heat transfer coefficient is calculated as $708.30 W/(m^2 K)$ on the coolant channel contact. By performing the transient state model analysis, the temperature behavior of the battery module is recorded, the temperature result at any time point of any component can be retrieved. As a demonstration, the FEA thermal images of the middle cell surface and the battery module at the peak temperature rise of 1C, 3C, 5C ultra-fast charging are presented, the temperature profiles of the global maximum on the cell, the global minimum on the plastic sheet, and the average are shown.

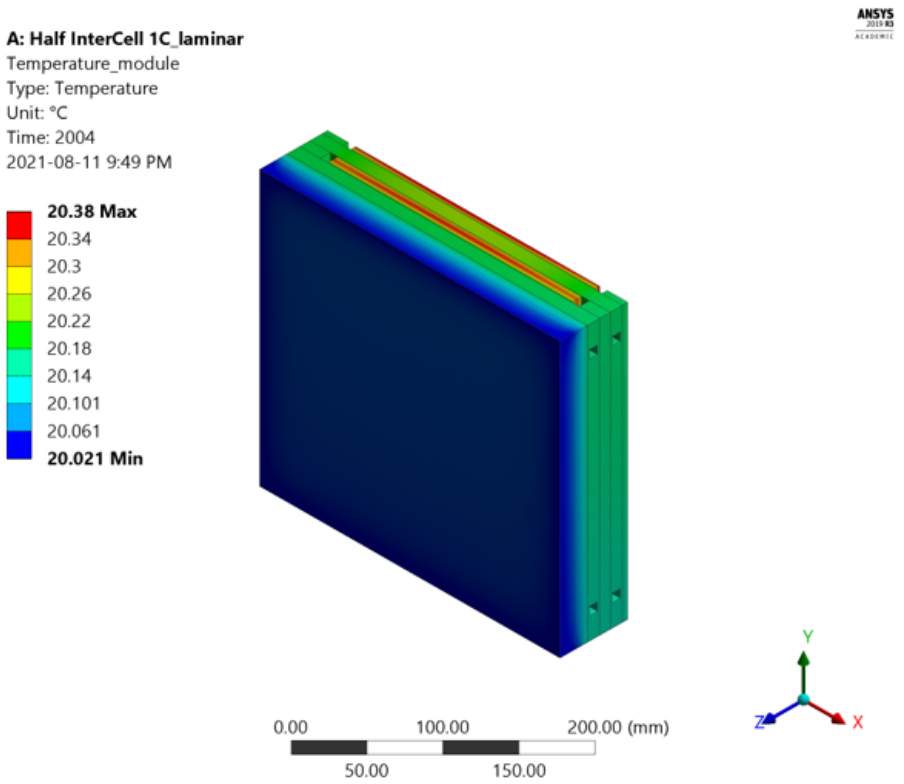

(a) FEA thermal image of the battery module at the peak temperature rise of 1C ultra-fast charging, peak temperature is 20.38°C at the top surface center of the middle cell

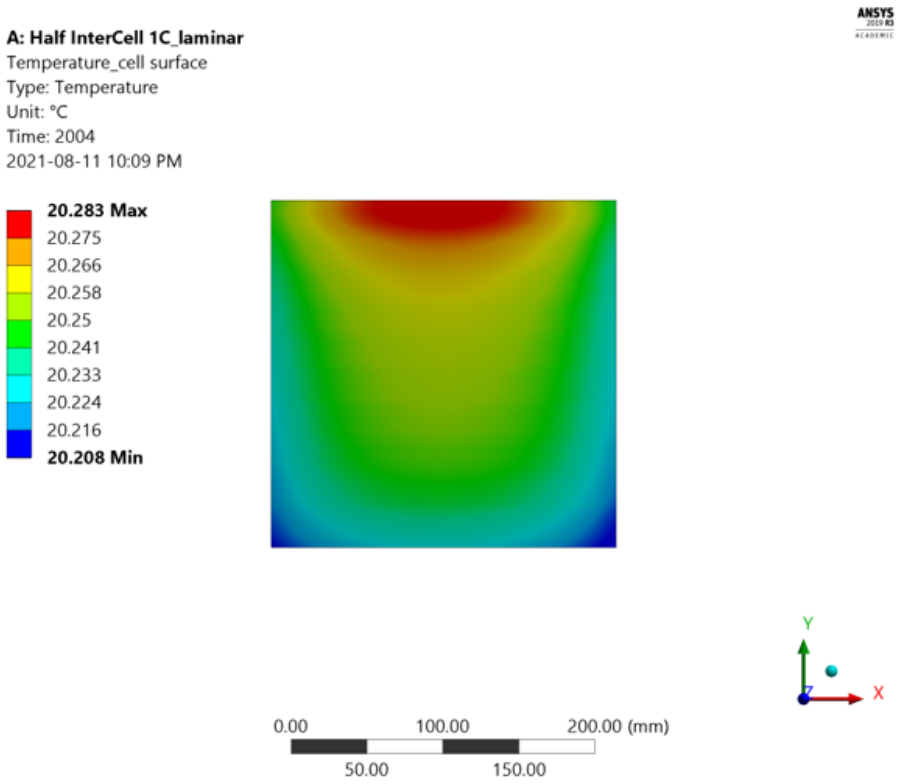

(b) FEA thermal image of the middle cell surface at the peak temperature rise of 1C ultra-fast charging, peak temperature is 20.283°C at the center of the top edge

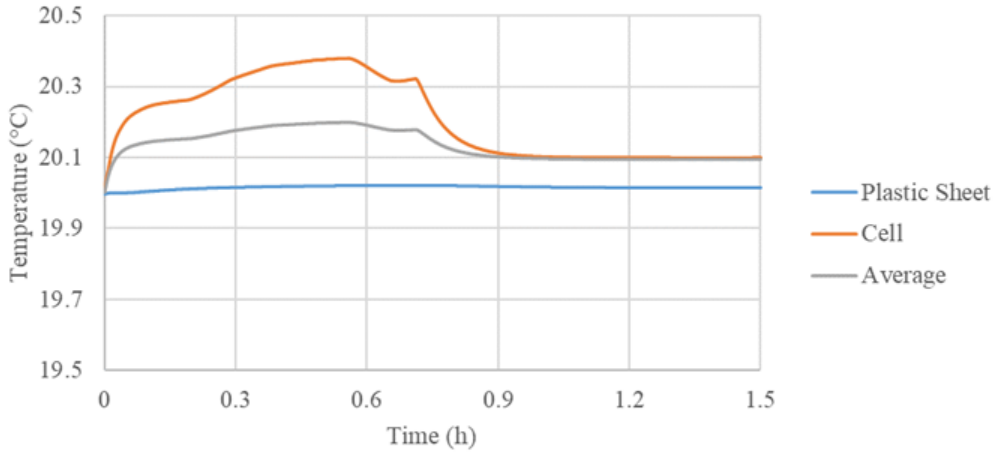

(c) Simulated temperature profiles of the global maximum on the cell, the global minimum on the plastic sheet, and the average under 1C ultra-fast charging

Figure 6.2: FEA thermal images and temperature profiles of 1C ultra-fast charging test simulation

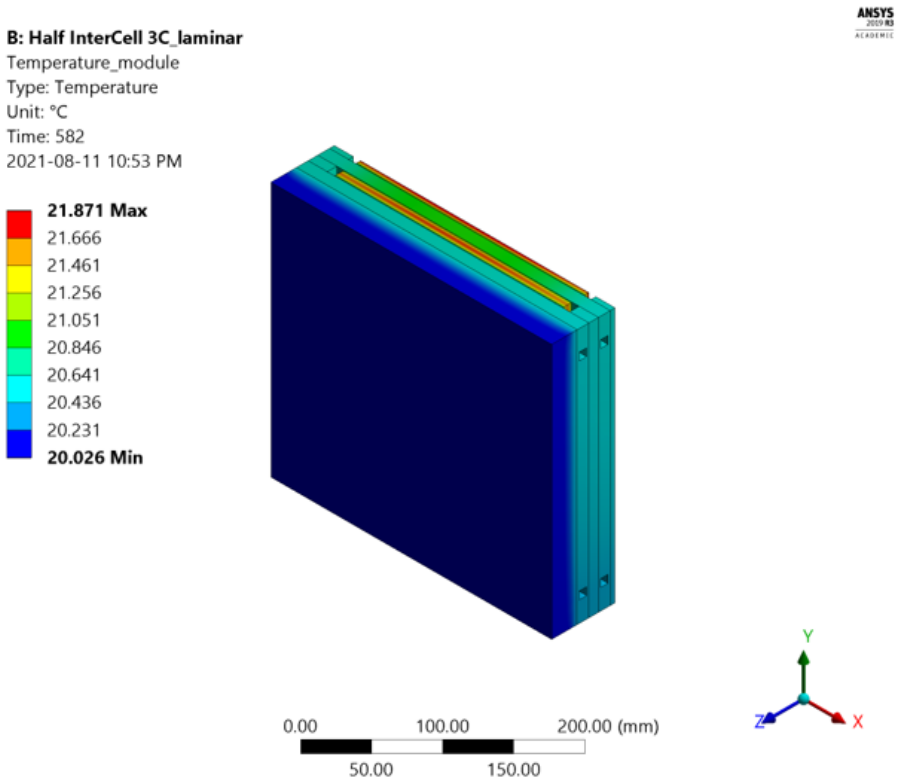

(a) FEA thermal image of the battery module at the peak temperature rise of 3C ultra-fast charging, peak temperature is 21.871°C at the top surface center of the middle cell

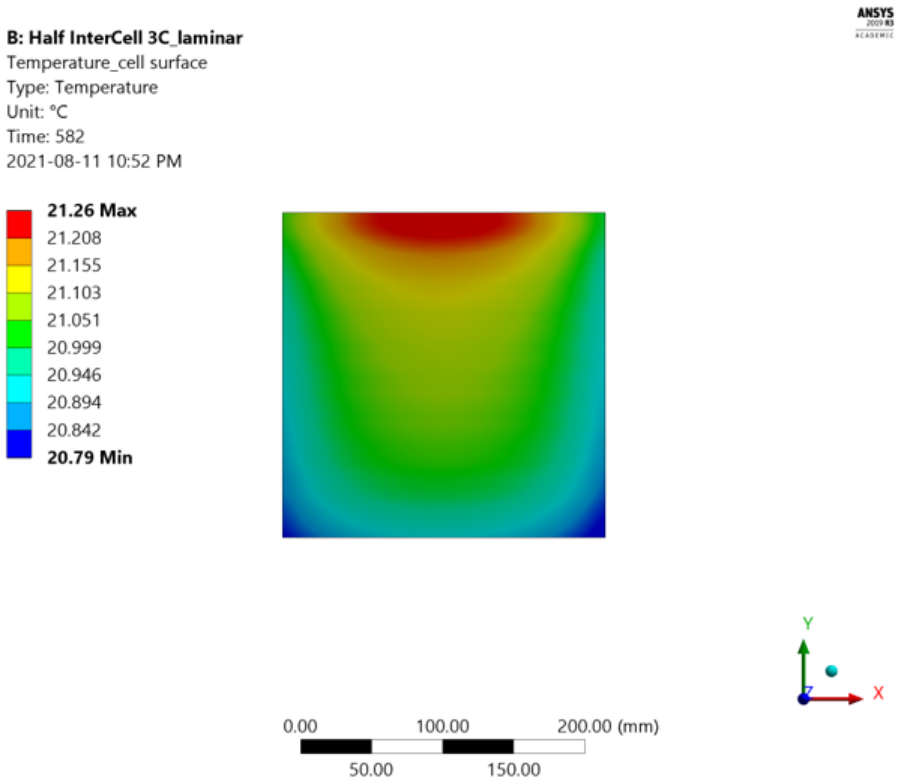

(b) FEA thermal image of the middle cell surface at the peak temperature rise of 3C ultra-fast charging, peak temperature is 21.26°C at the center of the top edge

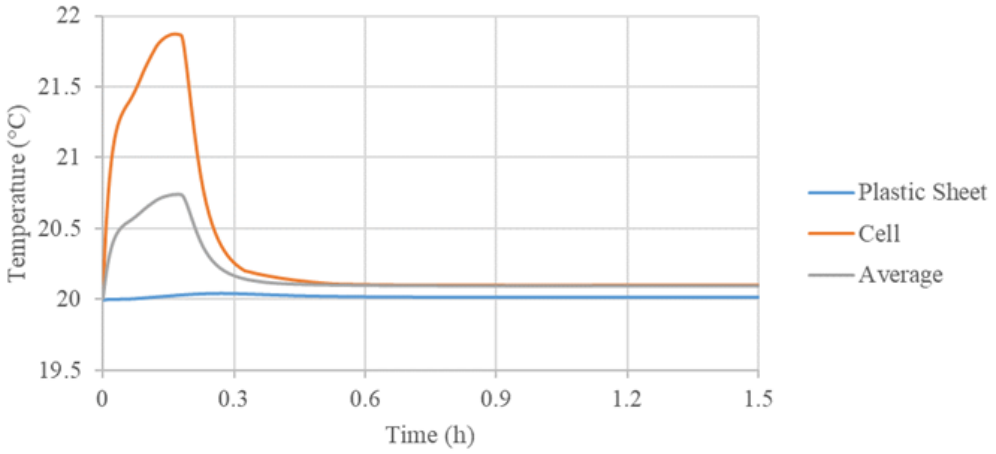

(c) Simulated temperature profiles of the global maximum on the cell, the global minimum on the plastic sheet, and the average under 3C ultra-fast charging

Figure 6.3: FEA thermal images and temperature profiles of 3C ultra-fast charging test simulation

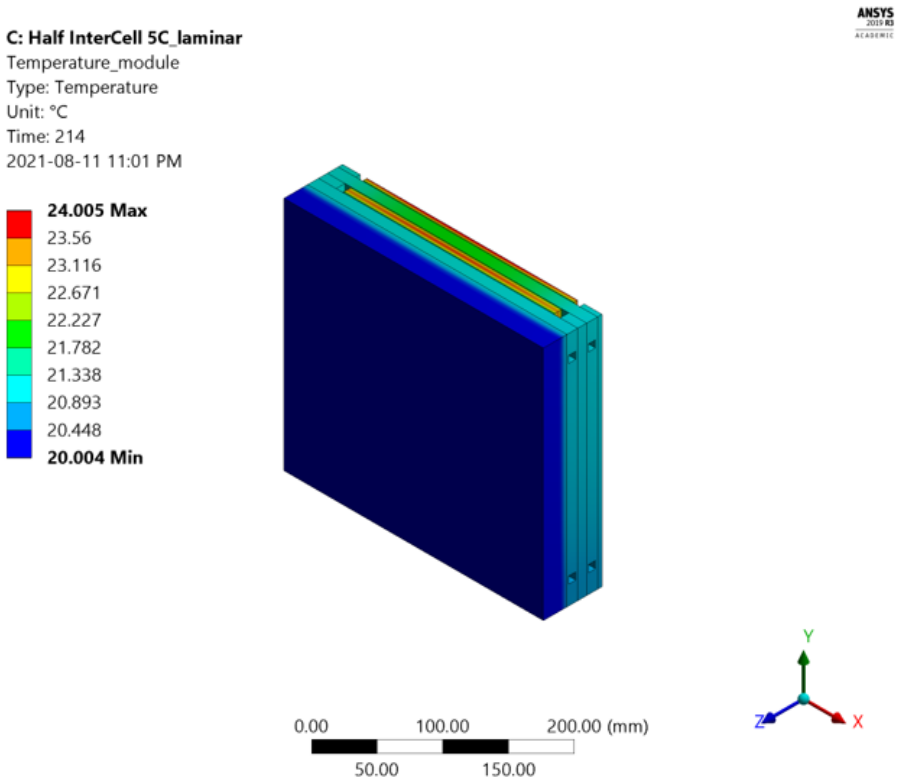

(a) FEA thermal image of the battery module at the peak temperature rise of 5C ultra-fast charging, peak temperature is 24.005°C at the top surface center of the middle cell

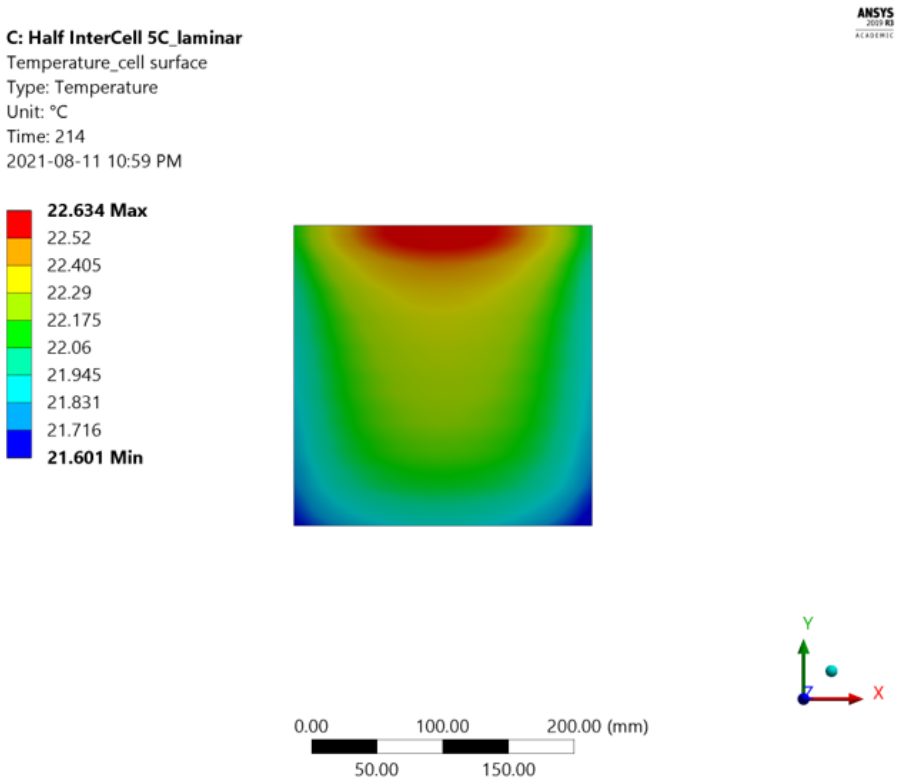

(b) FEA thermal image of the middle cell surface at the peak temperature rise of 5C ultra-fast charging, peak temperature is 22.634°C at the center of the top edge

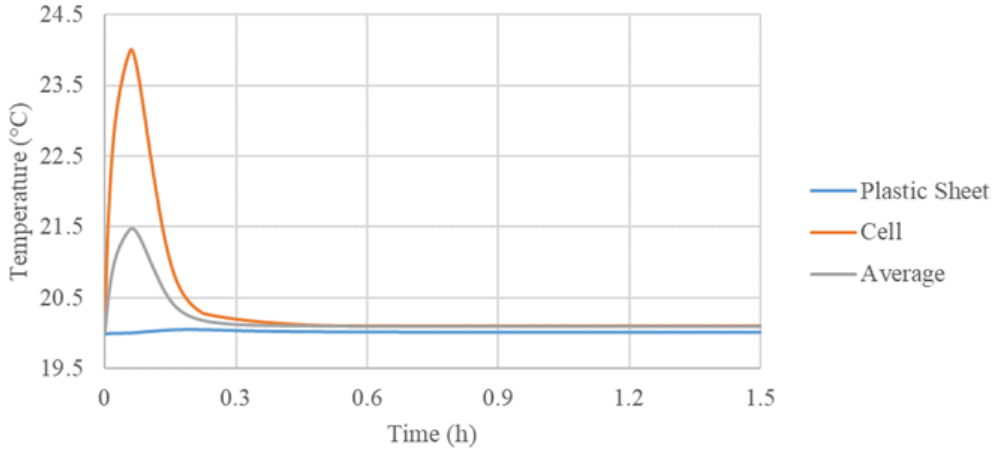

(c) Simulated temperature profiles of the global maximum on the cell, the global minimum on the plastic sheet, and the average under 5C ultra-fast charging

Figure 6.4: FEA thermal images and temperature profiles of 5C ultra-fast charging test simulation

Even though the peak temperature on the cell surface occurs at the top edge center where the positive and negative tabs are, it is not due to that the particular position of the cell has a high heat generation. The heat generation rate is uniformly assigned to the cell, but the cell is not placed at the center of the cooling plates, and the coolant flow direction is not aligned with the battery. As a matter of fact, the top edges of the cells have less heat transfer by the coolants, therefore, a higher temperature is observed.

6.2.3 Road Trip Test Simulation

The road trip test simulation is similar to the ultra-fast charging test simulation, but the modeled battery loss as the input to the transient state model is for the road trip with repeated US06 drive cycles and 4C ultra-fast charging. The driving condition is emulated that an EV's batteries are drained by following the US06 drive cycle speed profile, then a constant current of 4C magnitude charges the batteries followed by a constant voltage charge. When the batteries are charged to around 85% to 90% SOC, the EV starts the US06 drive cycle again, this procedure is repeated three times.

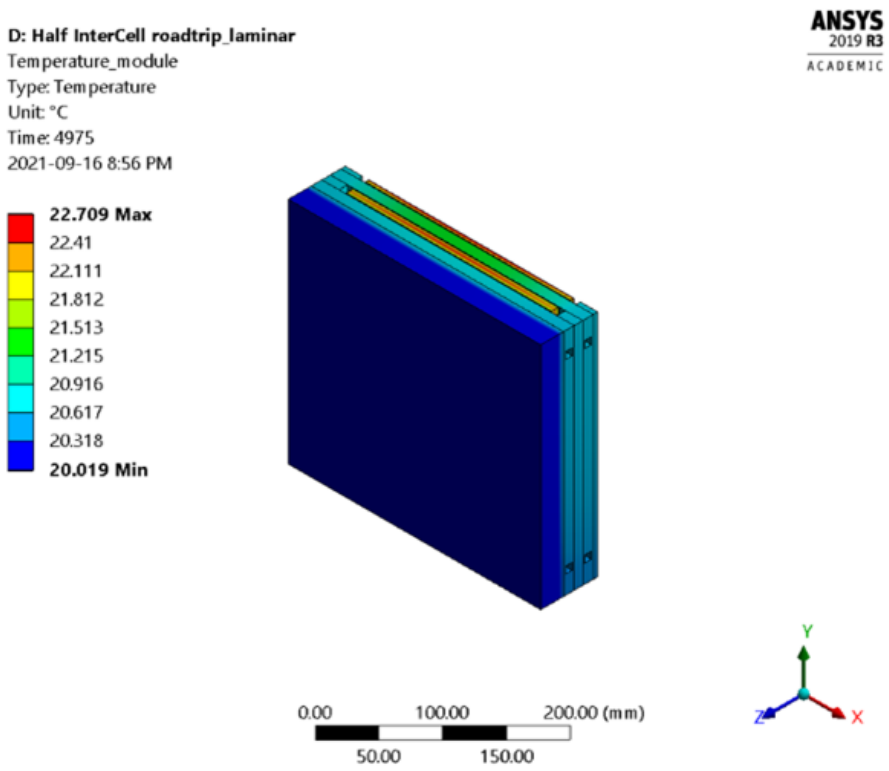

(a) FEA thermal image of the battery module at the peak temperature rise of road trip test, peak temperature is 22.709°C at the top surface center of the middle cell

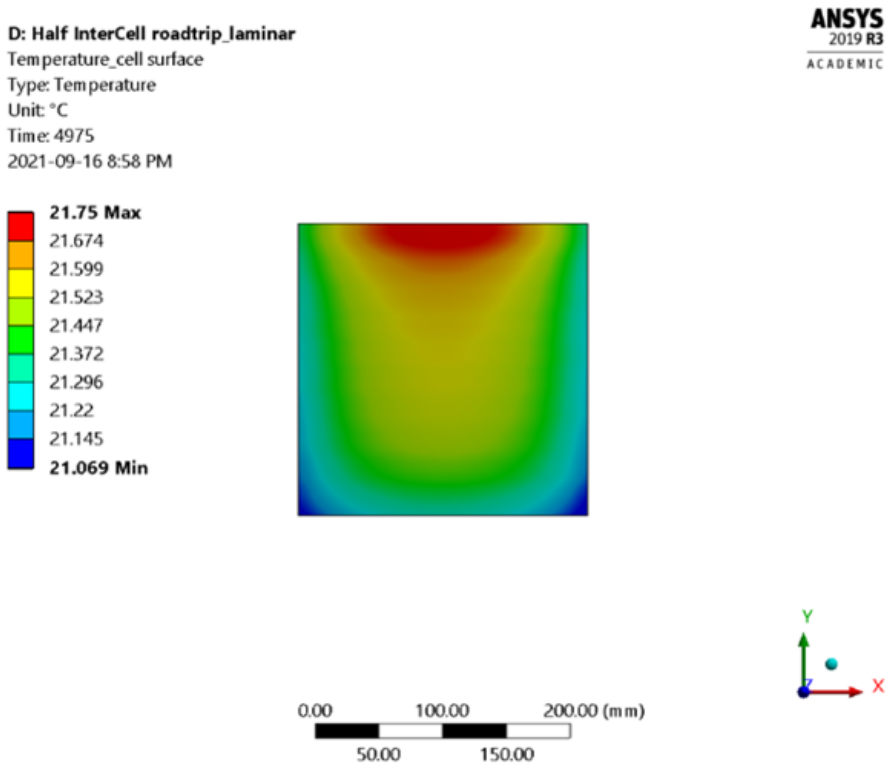

(b) FEA thermal image of the middle cell surface at the peak temperature rise of road trip test, peak temperature is 21.75°C at the center of the top edge

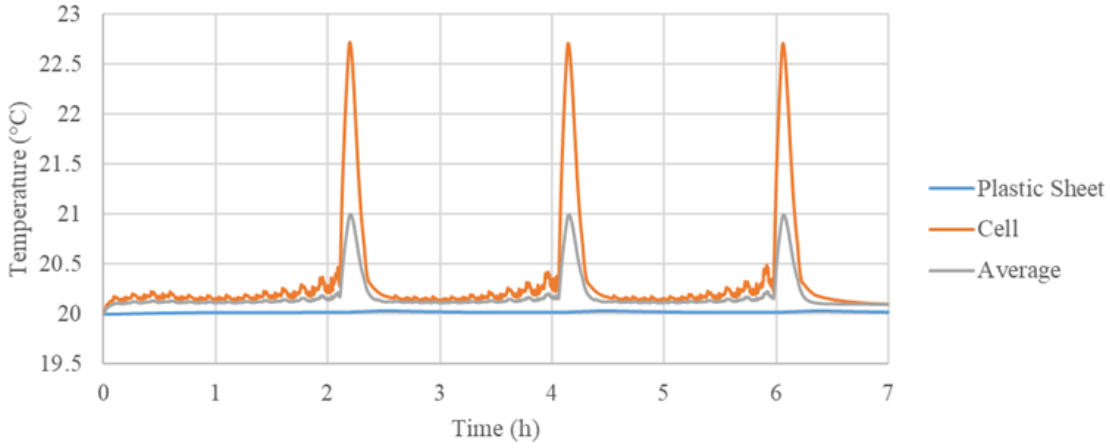

(c) Simulated temperature profiles of the global maximum on the cell, the global minimum on the plastic sheet, and the average under road trip test

Figure 6.5: FEA thermal images and temperature profiles of road trip test simulation

It is expected that the drive cycle part does not have an obvious temperature variation since it does not generate much heat. The peak temperature rise occurs during the 4C ultra-fast charging, and the temperature behavior of the battery module is similar to other ultra-fast charging tests, the peak temperature magnitude of the cell is between it of 3C and 5C cases.

6.3 Comparison of Thermal Modeling Results and Experiment Measurements

6.3.1 Thermal Resistance Comparison

Thermal resistance calculated in this work defines a lumped thermal property of how the battery module temperature changes with the battery loss. By comparing the thermal resistance of the FEA thermal models and the experimental measurements, the overall quality of the FEA thermal models can be predicted. There are five measured positions of the cell surface temperatures, while the thermal models cannot provide the temperatures of the corresponding positions due to the assumption of the uniform heat loss distribution over the cell surface and neglecting the cell terminals. The peak temperature occurs at the middle of the cell top edge in the thermal models, nonetheless, it is measured to be close to the negative tab in the experiment. To give a fair comparison, the average values of the measured top right and top left steady temperature state data are used for the thermal resistance calculation of the battery module, therefore, it can align with the peak temperature of the cell in the thermal models.

Table 6.2: Thermal resistance test comparison, initial temperature is 20°C, measurement is the average of top right and top left temperature rise

Measured Power Loss	Peak Temperature Rise of the Cell (°C)		Measurement (°C)
	Steady State Model	Transient State Model	
1.5C Test - 4W per cell	0.21	0.27	0.29
2C Test - 7W per cell	0.37	0.39	0.59
2.5C Test - 10W per cell	0.53	0.52	0.93
3C Test - 15W per cell	0.79	0.73	1.34
3.5C Test - 19W per cell	1.00	0.90	1.82

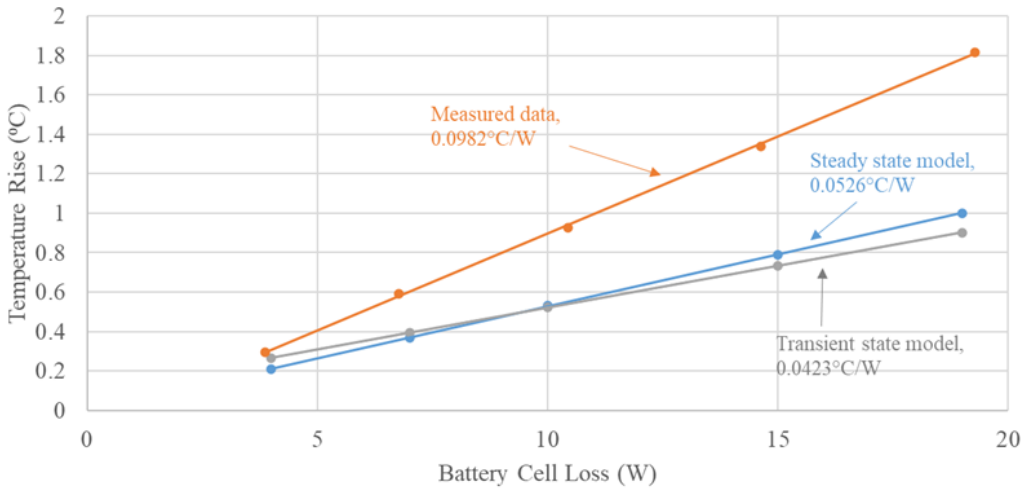

Figure 6.6: Thermal resistance calculation and comparison

From the table and figure, it can be seen that there are few discrepancies between the steady state model and the transient state model, and both FEA thermal models give under-predicted results compared with the experimental measurements. The main difference between the steady state model and the transient state model is the

neglect of coolant flow dynamics simulation, although this has many advantages of computation time. It is noticeable that the numerical simulations give over 50% error of the thermal resistance than the measured data, there are several reasons to account for the consequence. Some thermal properties such as the thermal conductivities of the battery and the thermal pads are not accurate in the thermal models, and no contact loss is considered in the battery module components. More importantly, the loss model contributes some errors because of the simplification and the uniformity assumption. In addition, there is a large amount of heat loss at the battery terminal connection in parallel, an increased contact area between the battery tabs improves the connection, but a large surface area leads to more heat dissipation to the environment. These under-predicted numerical simulation results of thermal resistance tests indicate lower temperature rises of the following simulations of ultra-fast charging tests and road trip tests compared to the experimental measurements.

6.3.2 Ultra-Fast Charging Temperature Comparison

The validation of the transient state model under 1C, 3C, 5C ultra-fast charging was performed in the previous section, the peak temperature profiles of the cells were collected. As mentioned in the thermal resistance test comparison, there is no measured data matched to the simulated peak temperature, so the simulated peak temperature is compared with the average value of the measured top right and top left temperatures on the cell surface. Moreover, the steady temperature state of the ultra-fast charging test during the numerical simulation is 20.1°C which is the estimated bulk-mean coolant temperature, while the measured temperature is around 19.9°C. Thus,

the modeled temperature is adjusted by subtracting this difference. Finally, the comparison of 1C, 3C, 5C ultra-fast charging tests between the numerical simulation and the experimental measurement is presented in Figure 6.7 and Table 6.3. Overall, the thermal model can give an accurate prediction of the battery temperature behavior under ultra-fast charging tests especially at a low charging C rate. The error of peak temperature is less than 0.1°C for a 1C charging, and the errors of high C-rate charging are less than 0.6°C.

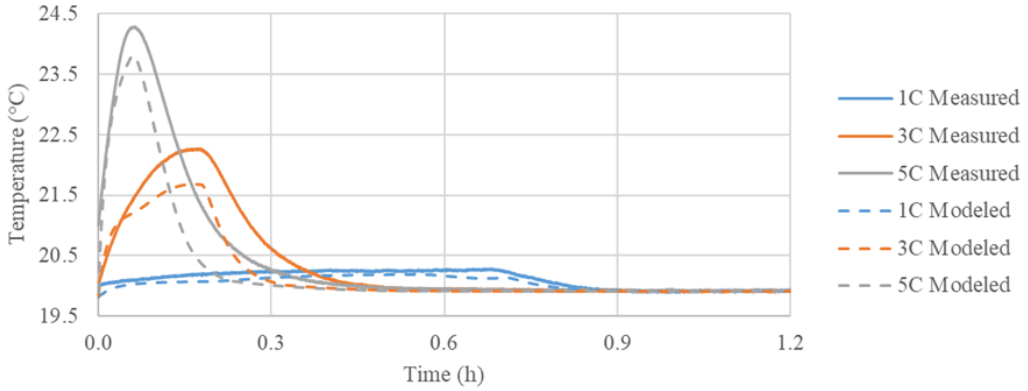

Figure 6.7: Ultra-fast charging temperature comparison

Table 6.3: Comparison of ultra-fast charging test peak temperatures

	Peak Temperature (°C)		
	1C	3C	5C
Numerical Simulation	20.19	21.68	23.82
Experimental Measurement	20.28	22.27	24.29
Deviation from Measurement (°C)	-0.09	-0.59	-0.47

6.3.3 Road Trip Temperature Comparison

Both modeled and measured temperature profiles are flat during the drive cycle part due to a negligible heat generation from the batteries, and the 4C charging part has an

evident temperature rise. The modeled peak temperature during 4C charging in the road trip test is 22.519°C, a reasonable value between the modeled 3C and 5C charging peak temperature, however, the deviation from the measured peak temperature, 1.158°C, is much higher than the deviation of 3C or 5C ultra-fast charging case which is less than 0.6°C. As indicated in the thermal resistance test, the thermal resistance of the transient state model is more than 50% smaller than it of the measured data, so the transient state model has a much faster thermal response than the experiment. Different from the ultra-fast charging test, the 4C charging part in the road trip test has a heat accumulation from the drive cycle part. From Figure 6.8, before the beginning of the 4C charging part, there is a slightly larger amount of heat generation at the low SOC state, which causes more heat accumulation to the 4C charging part in the experiment. While the thermal model has a smaller thermal resistance, the heat is less possible to accumulate so that the peak temperature is somewhat lower. In general, the thermal model can successfully predict the temperature behavior of the battery under a road trip test, this method can assess the modeled cooling system as a practical application.

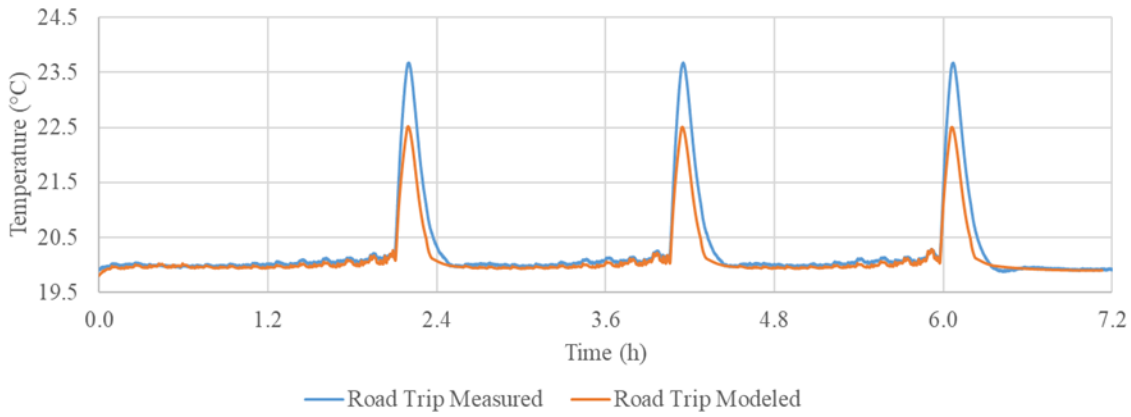

Figure 6.8: Road trip temperature comparison

6.4 Summary

The FEA thermal models including the steady state model and transient state model were validated with the thermal resistance tests, and the results were compared with the measured data from experiments. Generally, the thermal resistances of the FEA thermal models were around half of the measured data, which indicated that the thermal modeling would give an under-predicted estimation of the battery module temperature. Furthermore, the ultra-fast charging tests with 1C, 3C, 5C rates and the road trip test were validated on the transient state model. The peak temperature of the 1C charging test simulation was 0.1°C less than the measured data, and 0.6°C less for the 5C charging test simulation. The road trip test simulation gave a higher error that 1.158°C lower peak temperature than the experiment was observed. As a consequence, the thermal models can provide a good temperature estimation for the battery module as a guidance for further experimental work.

Chapter 7

Conclusions and Future Work

7.1 Summary of the Thesis

This thesis explored the thermal management system design of an ultra-fast charging battery module as the application on EVs. Both experiment and numerical simulation methods were taken to investigate the performance of the TMS qualitatively and quantificationally. The novel contributions of the work included comparing two liquid cooling systems designed for a battery module by experimental measurements, building and validating the FEA thermal model for one of the liquid cooling systems. Thereinto, battery fundamental knowledge involving battery definitions, ultra-fast charging techniques, battery testing skills, as well as heat transfer and thermodynamics theory served as the solid foundation of the work.

Starting with the literature review, ultra-fast charging to the EV battery had three main degradation mechanisms: lithium plating, electrolyte decomposition, and particle cracking. All the degradation mechanisms showed a strong relation to the battery temperature, which led to a further review of the battery TMS. Compared

with the air cooling method and phase change cooling method, the liquid cooling method had a better cooling efficiency and occupies less volume, thus widely applied in the automotive industry. Therefore, this thesis aimed to study the performance of ultra-fast charging battery modules with a liquid cooling method.

With three Kokam NMC 31 Ah pouch cells, two liquid cooling modules were designed according to a different heat flow schematic. The edge cooling module utilized coolant flowing through the cold plates along the edges of the battery module, and the inter-cell cooling module had the cold plates inserted between the cells. Then a set of tests were designed and carried out on the battery modules to compare the cooling performance. It was observed that the inter-cell cooling module had a much lower thermal resistance and controlled temperature much more efficiently. A series of ultra-fast charging tests with up to 5C rate were performed, the temperature of the edge cooling module increased 14.2°C for the highest charge rate, while the inter-cell cooling module had just 4.1°C temperature rise. In a similar manner, the peak temperature rise of the inter-cell module during a road trip test with a 4C charging was 3.4°C, and the edge cooling module had 12.2°C. Apparently, the configuration of the liquid cooling system played a crucial role in the thermal behavior of the battery module. The inter-cell cooling layout showed a competent cooling effect allowing for a higher coolant temperature or even higher ultra-fast charging C rate. Nevertheless, the complex inter-cell cooling configuration brought out many obstacles when fabricating, assembling, and sealing the cooling plates, these facts give rise to a higher manufacturing cost.

Afterward, thermal modeling of the inter-cell cooling module was developed as a benchmark against the experimental measurement. The battery heat generation

rate including both reversible loss and irreversible loss was calculated based on the simplified Bernardi heat generation model. The cell losses of difference C rates ultra-fast charging and a road trip were simulated to be consistent with the experimental tests and serve as the thermal model inputs. The CAE-based thermal models were established in ANSYS and distinguished by steady state model and transient state model. The CFD-based steady state model provided a more detailed calculation of the coolant flow so as to compute the heat transfer coefficient on the interface of the coolant and the channels of the cooling plates. Then the thermal-only transient state model used the heat transfer coefficient and the time-varying cell loss magnitude to simulate the temperature behavior of the battery module. A mesh sensitivity study was conducted on the thermal models so that the meshing with less than 5% error and fair computation time was employed for the simulation validation.

In terms of the validation of the FEA thermal models, the test plan was designed to characterize the thermal models and align with the experiment. Thermal resistance tests were performed to check the overall modeling quality, ultra-fast charging tests with 1C, 3C, 5C rates, and the road trip test with repeated US06 drive cycles and 4C charging gave an intuitional comparison. In general, the thermal resistances of the steady state model and the transient state model were around 50% deviating from the experimental measurements, this explained that the thermal models would have an under-predicted temperature estimation for the rest test simulations. As for the ultra-fast charging test simulations, the peak temperature of the 1C charging was 0.1°C lower than the measured data, while the high C-rate simulations had larger errors. The 3C charging case had the peak temperature of 21.68°C and 0.59°C lower than the measurement, the 5C charging case was 23.82°C, 0.47°C lower than

the experiment. Alike to the actual testing, the road trip simulation had neglectable temperature variation during the drive cycle part and a similar behavior with the ultra-fast charging simulation for the 4C charging part. The modeled peak temperature was 22.59°C which was 1.09°C lower than the experimental measurement. Given these points, the thermal models established for the inter-cell cooling battery module are able to provide an accurate temperature estimation, hence they are applicable for further test design prior to experimental validation.

7.2 Recommendations and Future Work

The inter-cell cooling battery module presented a strong cooling effect in both experiment and numerical simulation so that the temperature rise under a high C rate charging could be controlled within 5°C. However, the design in this thesis is too idealized to be massively produced in the industry. The cooling plates were machined by stamping the coolant channel and bonding thin aluminum plates together, while it is very hard to be manufactured. As for building a more pragmatic liquid cooling system that can be applied on a battery pack level, small-diameter coolant pipes cast into the metal can be adopted to reduce the weight and volume.

In addition, the chiller used in this work has a preponderant pump power and refrigerating capacity, a passenger vehicle cannot provide a chilling system with hundreds of Watts on three cells and circulating the coolant at 10L/min flow rate. As a potential future work of the research with the existing apparatus, piston valves or something similar can be designed on the hose network to control the coolant flow rate to a practical amount. Notably, simulations with a varied coolant flow rate can be designed on the thermal models, with a given cell loss or ultra-fast charging, the

relation between the coolant flow rate magnitude and the peak temperature rise of the battery can be derived. Furthermore, this empirical relation can be readily scaled to a pack level to determine the required pump power for regulating the battery within the desired operating temperature.

It was pointed out in Chapter 6, there are several ideas to improve the accuracy of the thermal modeling. The battery heat generation model is in a simplified form and has few connections with the battery material and property. In spite of a good loss estimation on the cylindrical cell, the pouch cell has a larger format thus having large temperature deviation across the surface, while the loss model assumed a uniform cell loss and ignored position-varying heat generation by the current density. Further experiments can be designed by placing heat flux sensors or measuring temperature drop across the thermal pads to derive a temperature/heat flux gradient function on the cell surface. Therefore, the thermal modeling applied with this gradient function can capture more thermal dynamics of the cell.

This thesis did not consider the loss at the cell tabs, as a matter of fact, there is quite a large proportion of heat generated at the battery terminals. Regarding the measurement of the cell tab losses, the terminal clamping can be machined with a configuration deep enough to cause an evident temperature drop, and the connection should be well insulated. With the known thermal properties of the clamping material and the measured temperature drop, the loss from the cell tabs can be calculated.

As for the minor errors of the thermal modeling, the thermal properties of the Kokam NMC cell were not acquired from the manufacturer specification, it was scaled by the density ratio of a battery with similar chemistry. Moreover, the thermal properties of the thermal pads and the aluminum might be slightly different from the

standard values due to pressure and temperature. In particular, the thermal modeling assumed a perfect contact between all the components and having no contact loss. If a higher simulation accuracy is required, an estimated or measured contact loss can be assigned to the models to improve the under-predicted thermal modeling.

References

Ahmed, R. (2014). *Modeling and state of charge estimation of electric vehicle batteries*. Ph.D. thesis.

Andwari, A. M., Pesiridis, A., Rajoo, S., Martinez-Botas, R., and Esfahanian, V. (2017). A review of battery electric vehicle technology and readiness levels. *Renewable and Sustainable Energy Reviews*, **78**, 414–430.

ANSYS (2009). Ansys fluent 12.0 theory guide. https://www.afs.enea.it/project/neptunius/docs/fluent/html/th/main$_p re.htm$, [*Accessed* : *Aug*.2021].

ANSYS (2020). Intro to transient thermal analysis. https://courses.ansys.com/wp-content/uploads/2020/05/Lesson-1-Introduction-to-transient-analysis.pdf, [Accessed: Aug. 2021].

Battery University (2018a). Bu-104b: Battery building blocks. https://batteryuniversity.com/article/bu-104b-battery-building-blocks, [Accessed: Aug. 2021].

Battery University (2018b). Bu-204: How do lithium batteries work?

https://batteryuniversity.com/article/bu-204-how-do-lithium-batteries-work, [Accessed: Aug. 2021].

Battery University (2019a). Bu-201: How does the lead acid battery work? https://batteryuniversity.com/article/bu-201-how-does-the-lead-acid-battery-work, [Accessed: Aug. 2021].

Battery University (2019b). Bu-203: Nickel-based batteries. https://batteryuniversity.com/article/bu-203-nickel-based-batteries, [Accessed: Aug. 2021].

Battery University (2019c). Bu-205: Types of lithium-ion. https://batteryuniversity.com/article/bu-205-types-of-lithium-ion, [Accessed: Aug. 2021].

Battery University (2019d). Bu-908: Battery management system (bms). https://batteryuniversity.com/article/bu-908-battery-management-system-bms, [Accessed: Aug. 2021].

Bernardi, D., Pawlikowski, E., and Newman, J. (1985). A general energy balance for battery systems. *Journal of the electrochemical society*, **132**(1), 5.

BioLogic (2021). Anode, cathode, positive and negative: battery basics. https://www.biologic.net/topics/anode-cathode-positive-and-negative-battery-basics/, [Accessed: Aug. 2021].

Bower, G. (2015). Tesla or gm: Who has the best battery thermal management? https://insideevs.com/news/328909/tesla-or-gm-who-has-the-best-battery-thermal-management/, [Accessed: Aug. 2021].

Chalk, S. G. and Miller, J. F. (2006). Key challenges and recent progress in batteries, fuel cells, and hydrogen storage for clean energy systems. *Journal of Power Sources*, **159**(1), 73–80.

CWG (1991). Properties of mixture water/glycol. https://detector-cooling.web.cern.ch/data/Table%208-3-1.htm, [Accessed: Aug. 2021].

Doll, S. (2021). Electric vehicle (EV) charging standards and how they differ. https://electrek.co/2021/07/21/electric-vehicle-ev-charging-standards-and-how-they-differ/#h-sae-j1772, [Accessed: Aug. 2021].

Easy Electric Cars (2019). Why do tesla batteries not overheat? tesla's battery cooling system. https://www.easyelectriccars.com/why-do-tesla-batteries-not-overheat-teslas-battery-cooling-system/, [Accessed: Aug. 2021].

Giuliano, M. R., Prasad, A. K., and Advani, S. G. (2012). Experimental study of an air-cooled thermal management system for high capacity lithium–titanate batteries. *Journal of power sources*, **216**, 345–352.

Green Car Congress (2017). Audi unveils q8 plug-in hybrid concept full-size suv; production version in 2018. https://www.greencarcongress.com/2017/01/20170109-q8.html, [Accessed: Aug. 2021].

He, M. (2018). *Testing, Characterization, and Thermal Analysis of Lithium-Ion Batteries Toward Battery Pack Design for Ultra-Fast Charging.* Ph.D. thesis.

He, M. S., Kollmeyer, P. J., Haußmann, M., and Emadi, A. (2018). A comparison of the performance and thermal management requirements of lithium-ion batteries

during ultra-fast charging. In *2018 IEEE Transportation Electrification Conference and Expo (ITEC)*, pages 675–680. IEEE.

Hein, S. and Latz, A. (2016). Influence of local lithium metal deposition in 3d microstructures on local and global behavior of lithium-ion batteries. *Electrochimica Acta*, **201**, 354–365.

Hu, X., Li, S., and Peng, H. (2012). A comparative study of equivalent circuit models for li-ion batteries. *Journal of Power Sources*, **198**, 359–367.

Hussein, A. A.-H. and Batarseh, I. (2011). An overview of generic battery models. In *2011 IEEE Power and Energy Society General Meeting*, pages 1–6. IEEE.

Jaguemont, J., Omar, N., Van den Bossche, P., and Mierlo, J. (2018). Phase-change materials (pcm) for automotive applications: A review. *Applied thermal engineering*, **132**, 308–320.

Khateeb, S. A., Farid, M. M., Selman, J. R., and Al-Hallaj, S. (2004). Design and simulation of a lithium-ion battery with a phase change material thermal management system for an electric scooter. *Journal of Power Sources*, **128**(2), 292–307.

Khateeb, S. A., Amiruddin, S., Farid, M., Selman, J. R., and Al-Hallaj, S. (2005). Thermal management of li-ion battery with phase change material for electric scooters: experimental validation. *Journal of Power Sources*, **142**(1-2), 345–353.

Kokam (2016). Superior lithium polymer battery (slpb) kokam li-ion/polymer cell. https://kokam.com/wp-content/uploads/2016/03/SLPB-Cell-Brochure.pdf, [Accessed: Aug. 2021].

Kumar, M. S. and Revankar, S. T. (2017). Development scheme and key technology of an electric vehicle: An overview. *Renewable and Sustainable Energy Reviews*, **70**, 1266–1285.

Kurganov, V. (2011). Heat transfer coefficient. https://www.thermopedia.com/content/841/, [Accessed: Aug. 2021].

Lei, H. and Han, Y. Y. (2019). The measurement and analysis for open circuit voltage of lithium-ion battery. In *Journal of Physics: Conference Series*, volume 1325, page 012173. IOP Publishing.

Lempert, J., Kollmeyer, P., Malysz, P., Gross, O., Cotton, J., and Emadi, A. (2020). Battery entropic heating coefficient testing and use in cell-level loss modeling for extreme fast charging. *SAE International Journal of Advances and Current Practices in Mobility*, **2**(2020-01-0862), 2712–2720.

Liaw, B. Y., Nagasubramanian, G., Jungst, R. G., and Doughty, D. H. (2004). Modeling of lithium ion cells—a simple equivalent-circuit model approach. *Solid state ionics*, **175**(1-4), 835–839.

Liu, Y., Zhu, Y., and Cui, Y. (2019). Challenges and opportunities towards fast-charging battery materials. *Nature Energy*, **4**(7), 540–550.

Lu, L., Han, X., Li, J., Hua, J., and Ouyang, M. (2013). A review on the key issues for lithium-ion battery management in electric vehicles. *Journal of power sources*, **226**, 272–288.

Malik, M., Dincer, I., and Rosen, M. A. (2016). Review on use of phase change materials

in battery thermal management for electric and hybrid electric vehicles. *International Journal of Energy Research*, **40**(8), 1011–1031.

Meng, J., Luo, G., Ricco, M., Swierczynski, M., Stroe, D.-I., and Teodorescu, R. (2018). Overview of lithium-ion battery modeling methods for state-of-charge estimation in electrical vehicles. *Applied sciences*, **8**(5), 659.

Moore, S. and Eshani, M. (1996). An empirically based electrosource horizon lead-acid battery model. *SAE transactions*, pages 421–424.

Mussa, A. S., Klett, M., Behm, M., Lindbergh, G., and Lindström, R. W. (2017). Fast-charging to a partial state of charge in lithium-ion batteries: A comparative ageing study. *Journal of Energy Storage*, **13**, 325–333.

Nieto, N., Díaz, L., Gastelurrutia, J., Blanco, F., Ramos, J. C., and Rivas, A. (2014). Novel thermal management system design methodology for power lithium-ion battery. *Journal of Power Sources*, **272**, 291–302.

Panchal, S., Mathewson, S., Fraser, R., Culham, R., and Fowler, M. (2015). Thermal management of lithium-ion pouch cell with indirect liquid cooling using dual cold plates approach. *SAE International Journal of Alternative Powertrains*, **4**(2), 293–307.

Pesaran, A. A. (2001). Battery thermal management in ev and hevs: issues and solutions. *Battery Man*, **43**(5), 34–49.

Pesaran, A. A. (2002). Battery thermal models for hybrid vehicle simulations. *Journal of power sources*, **110**(2), 377–382.

Plett, G. L. (2004). Extended kalman filtering for battery management systems of lipb-based hev battery packs: Part 3. state and parameter estimation. *Journal of Power sources*, **134**(2), 277–292.

Pokrzywa, J. (2011). Sae international standards work, including communication protocols and connectors, fast charge, batteries. *SAE International*.

Rao, Z. and Wang, S. (2011). A review of power battery thermal energy management. *Renewable and Sustainable Energy Reviews*, **15**(9), 4554–4571.

Schindler, S., Bauer, M., Cheetamun, H., and Danzer, M. A. (2018). Fast charging of lithium-ion cells: identification of aging-minimal current profiles using a design of experiment approach and a mechanistic degradation analysis. *Journal of Energy Storage*, **19**, 364–378.

Shim, J., Kostecki, R., Richardson, T., Song, X., and Striebel, K. A. (2002). Electrochemical analysis for cycle performance and capacity fading of a lithium-ion battery cycled at elevated temperature. *Journal of power sources*, **112**(1), 222–230.

Singh, K. V., Bansal, H. O., and Singh, D. (2019). A comprehensive review on hybrid electric vehicles: architectures and components. *Journal of Modern Transportation*, **27**(2), 77–107.

Smith, K. and Wang, C.-Y. (2006a). Power and thermal characterization of a lithium-ion battery pack for hybrid-electric vehicles. *Journal of power sources*, **160**(1), 662–673.

Smith, K. and Wang, C.-Y. (2006b). Solid-state diffusion limitations on pulse operation of a lithium ion cell for hybrid electric vehicles. *Journal of power sources*, **161**(1), 628–639.

Spotnitz, R. (2005). Advanced ev and hev batteries. In *2005 IEEE Vehicle Power and Propulsion Conference*, pages 4–pp. IEEE.

Srinivasan, V. and Wang, C. (2002). Analysis of electrochemical and thermal behavior of li-ion cells. *Journal of The Electrochemical Society*, **150**(1), A98.

Synergy Files (2018). A review of battery thermal management system. http://synergyfiles.com/2016/07/battery-thermal-management-system-review/, [Accessed: Aug. 2021].

Team, M. *et al.* (2008). A guide to understanding battery specifications. *Massachusetts Institute of technology, USA, Tech. Rep.*

Thomas, C. S. (2009). Transportation options in a carbon-constrained world: Hybrids, plug-in hybrids, biofuels, fuel cell electric vehicles, and battery electric vehicles. *International Journal of hydrogen energy*, **34**(23), 9279–9296.

Tomaszewska, A., Chu, Z., Feng, X., O'Kane, S., Liu, X., Chen, J., Ji, C., Endler, E., Li, R., Liu, L., *et al.* (2019). Lithium-ion battery fast charging: A review. *ETransportation*, **1**, 100011.

TWAICE (2019). Batteries explained - from cell formats to chemistries. https://twaice.com/articles-battery-technology/, [Accessed: Aug. 2021].

Unnewehr, L. E. and Nasar, S. A. (1982). Electric vehicle technology.

Verma, A., Singh, B., Chandra, A., and Al-Haddad, K. (2020). An implementation of solar pv array based multifunctional ev charger. *IEEE Transactions on Industry Applications*, **56**(4), 4166–4178.

Vetter, J., Novák, P., Wagner, M. R., Veit, C., Möller, K.-C., Besenhard, J., Winter, M., Wohlfahrt-Mehrens, M., Vogler, C., and Hammouche, A. (2005). Ageing mechanisms in lithium-ion batteries. *Journal of power sources*, **147**(1-2), 269–281.

Washington Edu (2021). Classification of cells or batteries. https://depts.washington.edu/matseed/batteries/MSE/classification.html, [Accessed: Aug. 2021].

Wikipedia (2021). Nickel-metal hydride battery. https://en.wikipedia.org/wiki/Nickel%E2%80%93metal_hydride_battery, [Accessed: Aug. 2021].

Wohlfahrt-Mehrens, M., Vogler, C., and Garche, J. (2004). Aging mechanisms of lithium cathode materials. *Journal of power sources*, **127**(1-2), 58–64.

Wu, W., Wang, S., Wu, W., Chen, K., Hong, S., and Lai, Y. (2019). A critical review of battery thermal performance and liquid based battery thermal management. *Energy conversion and management*, **182**, 262–281.

Xing, Y., He, W., Pecht, M., and Tsui, K. L. (2014). State of charge estimation of lithium-ion batteries using the open-circuit voltage at various ambient temperatures. *Applied Energy*, **113**, 106–115.

Ye, B., Rubel, M. R. H., and Li, H. (2019). Design and optimization of cooling plate for battery module of an electric vehicle. *Applied Sciences*, **9**(4), 754.

Zhang, S., Xu, K., and Jow, T. (2002). A new approach toward improved low temperature performance of li-ion battery. *Electrochemistry communications*, **4**(11), 928–932.

Zhang, S., Xu, K., and Jow, T. (2003). The low temperature performance of li-ion batteries. *Journal of Power Sources*, **115**(1), 137–140.

Zhao, L., Lin, M., and Chen, Y. (2016). Least-squares based coulomb counting method and its application for state-of-charge (soc) estimation in electric vehicles. *International Journal of Energy Research*, **40**(10), 1389–1399.